JOURNAL OF PETROLOGY

Journal of Petrology, 2015, Vol. 56, No. 9, 1775–1796
doi: 10.1093/petrology/egv054
Original Article

OXFORD

Metasomatism of the Lithospheric Mantle Immediately Precedes Kimberlite Eruption: New Evidence from Olivine Composition and Microstructures

Carole Cordier[1,2]*, Lucie Sauzeat[1,2†], Nicholas T. Arndt[1,2], Anne-Marie Boullier[1,2], Valentina Batanova[1,2] and Fabrice Barou[3]

[1]Université Grenoble Alpes, ISTerre, F-38041 Grenoble, France, [2]CNRS, ISTerre, F-38041 Grenoble, France and [3]Université Montpellier 2, Géosciences Montpellier, Place Eugène Bataillon, 34095 Montpellier, cedex 05, France

*Corresponding author. E-mail: carole.cordier@ujf-grenoble.fr
[†]Present address: CNRS UMR 5276, Laboratoire de Géologie de Lyon, Ecole Normale Supérieure de Lyon, Université Lyon 1, 69634 Lyon, France.

Received July 30, 2014; Accepted August 27, 2015

ABSTRACT

Most kimberlites contain abundant dunitic nodules. These are centimetre-sized, rounded and multi-grained assemblages of xenocrystic olivine with a wide range of compositions (Fo83 to Fo94). The absence of orthopyroxene and other mantle minerals and the range of olivine compositions have been attributed to reaction between mantle peridotite and (proto)kimberlitic fluid or melt, but the timing of the reaction is a subject of debate. In a kimberlite from the Kangamiut region of Greenland, nodule cores are surrounded by fine-grained outer margins with near-constant Fo contents (~Fo88) but highly variable minor element contents (e.g. 500–2500 ppm Ni). These margins crystallized from the kimberlite melt and we show that their compositions can be explained by crystallization of olivine alone, if a high partition coefficient for Ni between melt and olivine ($D_{Ni} > 20$) is assumed. Orthopyroxene assimilation is not required, removing the constraint that its dissolution occurred during ascent of the kimberlite magma. Within some nodules, in addition to the usual core-to-margin gradients, we observe asymmetric compositional changes (variable Fo but near-constant minor element contents) across mobile grain boundaries. These changes document fluid percolation at the grain scale that occurred during dynamic recrystallization in the deforming lithospheric mantle. We note that chemical gradients associated with mobile grain boundaries are observed in olivines that cover the entire compositional range of the nodules, and propose that fluid-assisted dynamic recrystallization took place in dunite that was already compositionally heterogeneous. Reaction between peridotite and protokimberlitic melt or fluid and dissolution of orthopyroxene thus occurred within the lithospheric mantle, immediately (a few days) prior to the ascent of the kimberlite melt and the entrainment of the dunite nodules. We propose that the grain boundary zones probably mimic, at a fine scale, the fluid–peridotite interaction that caused, at a larger scale, orthopyroxene dissolution and formation of compositionally diverse olivine in kimberlites.

Key words: dunite; grain boundary migration; kimberlite; olivine xenocryst; metasomatism

INTRODUCTION

For decades the olivine grains in kimberlites have been classified into two populations on the basis of their grain size and morphology; each type has been ascribed a different origin (Skinner & Clement, 1979; Clement, 1982; Mitchell, 1986, 2008; Moore, 1988, 2012; Le Roex *et al.*, 2003; Kopylova *et al.*, 2007; Kamenetsky *et al.*, 2008; Brett *et al.*, 2009; Arndt *et al.*, 2010). Much of the discussion has focused on the relative proportion of xenocrysts—olivine from another source, typically the lithospheric mantle—and phenocrysts—cognate olivine that crystallized directly from the kimberlite magma. In earlier publications the cores of larger grains, particularly when anhedral or rounded, were regarded as xenocrysts whereas smaller sub- to euhedral grains were regarded as phenocrysts (e.g. Mitchell, 1986; Moore, 1988, 2012; Kamenetsky *et al.*, 2008). More recently, it was proposed that almost all of the olivine grains in kimberlites are xenocrysts and that cognate olivine is restricted to thin rims around anhedral olivine cores (Fedortchouk & Canil, 2004; Brett *et al.*, 2009; Arndt *et al.*, 2010; Pilbeam *et al.*, 2013).

Another issue that has elicited discussion is the fate of orthopyroxene, clinopyroxene and garnet, minerals that make up close to 50% of most deep-seated mantle peridotites, but are rare to absent in kimberlites. It is generally accepted that these minerals, especially orthopyroxene (Luth, 2009), are out of equilibrium with the proto-kimberlitic liquid, which most probably is a CO_2–H_2O-rich, silica-poor fluid, and that these minerals reacted with or dissolved in this liquid. The question is when this happened. Most researchers (Kamenetsky *et al.*, 2008; Brett *et al.*, 2009, 2015; Russell *et al.*, 2012; Pilbeam *et al.*, 2013; Kamenetsky & Yaxley, 2015) consider that this dissolution took place in the kimberlite en route to the surface. Arndt *et al.* (2010), however, proposed that the removal of mantle minerals other than olivine took place within the mantle lithosphere, producing dunites that subsequently were entrained into the kimberlite magma.

We present here a geochemical and microstructural study of olivine in a very well-preserved type-I kimberlite from the Kangamiut region in Greenland. We document in detail the variations in forsterite content as well as minor element contents in the olivine grains in this sample, in particular across the outer margins of grains and across internal grain boundaries in multigranular nodules. Combining microstructural evidence for dynamic recrystallization at mantle depths with evidence for chemical gradients across grain boundaries, we develop firm constraints on the timing and location of the processes that removed orthopyroxene, and clarify several important issues concerning the migration of kimberlitic magmas in the lithospheric mantle.

OLIVINE IN KIMBERLITES: LITERATURE REVIEW

Types of olivine grains

The eruptive facies in kimberlite pipes are breccias that contain abundant rock fragments. They are usually totally altered to secondary hydrous phases; however, some hypabyssal samples are well preserved. Fresh kimberlites contain abundant large grains of olivine that have been described using the terms listed in Table 1 and illustrated in Fig. 1. The large rounded grains that dominate the lithology of most samples are commonly referred to as 'macrocrysts' or 'megacrysts' (Clement, 1982; Mitchell, 1986), or more recently as 'olivine-I' (Kamenetsky *et al.*, 2008). These terms do not adequately depict their rounded form, nor do they accommodate their polycrystalline structure. For these reasons, we prefer to use the term 'nodule' (Arndt *et al.*, 2010). We emphasize that the objects described by this term are distinct from normal peridotite xenoliths; that is, fragments of mantle peridotite plucked from conduit walls and transported to the surface in the kimberlite magma. Whereas nodules in kimberlites are typically less than 1 cm across and almost always monomineralic, peridotite xenoliths are larger (2 cm or more) and mainly multimineralic; that is, they normally contain ortho- and clinopyroxene and an aluminous phase (garnet or spinel) in addition to olivine.

Olivine nodules in kimberlites are typically well rounded, with an average size <1 cm. Many are monogranular, but others are multigranular and consist of two of more large grains of anhedral olivine (Fig. 1). Many anhedral olivines exhibit abundant high-temperature and high-stress intracrystalline deformation features such as undulose extinction and subgrain dislocation walls (Boullier & Nicolas, 1975; Guéguen, 1977; Skinner, 1989; Arndt *et al.*, 2010). Some grains also show evidence for dynamic recrystallization at mantle depths with the development of small equigranular mosaic-textured and dislocation-rich grains (Arndt *et al.*, 2010). Little-deformed subhedral to euhedral crystals (tablets), which occur within many nodules, are thought to derive from deformed anhedral olivine by fluid-assisted static recrystallization (i.e. post-deformation annealing), during the first stage of upward migration of the kimberlite magma to the surface (Guéguen, 1977, 1979; Drury & van Roermund, 1988, 1989; Nermond, 1994). The size of single crystals in kimberlite nodules may reach 8–10 mm, greater than the typical grain size in peridotite xenoliths (<8 mm; Mercier & Nicolas, 1975).

The small, euhedral to rounded crystals in the kimberlite matrix have been called 'phenocrysts' by Clement (1982), 'olivine-II' by Kamenetsky *et al.* (2008) and 'matrix olivine' by Arndt *et al.* (2010). Some matrix olivine cores show dislocation microstructures similar to those in anhedral olivines, but others have an asymmetric, subhedral morphology very similar to that of tablets. Matrix grains are thus interpreted to result from disaggregation of larger xenocrystic nodules during kimberlite ascent (Brett *et al.*, 2009; Arndt *et al.*, 2010).

Olivine composition and nomenclature

A striking feature of the olivine grains in kimberlites is the wide range of core compositions from nodule to

Table 1: Nomenclature of olivine in kimberlites

Name	Components	Microstructures	Interpretation
Nodule (macrocrysts, olivine-I)* large, rounded, multi- or monomineralic	Anhedral, 1 to > 50 mm	Undulose extinction High dislocation density (walls + free dislocation)	Xenocrysts produced by metasomatism and deformation in the lithospheric mantle
	Mosaic-textured, <0·1 mm grains		Dynamically recrystallized grains
	Tablet, 0·3–1 mm	Low dislocation density	Static recrystallization during kimberlite ascent
Matrix olivine (phenocrysts, olivine-II)* small, euhedral to rounded in the kimberlite matrix	0·3–1 mm	High or low dislocation density	Disaggregated nodules (tablets or anhedral olivines)

*Terms used in the literature.

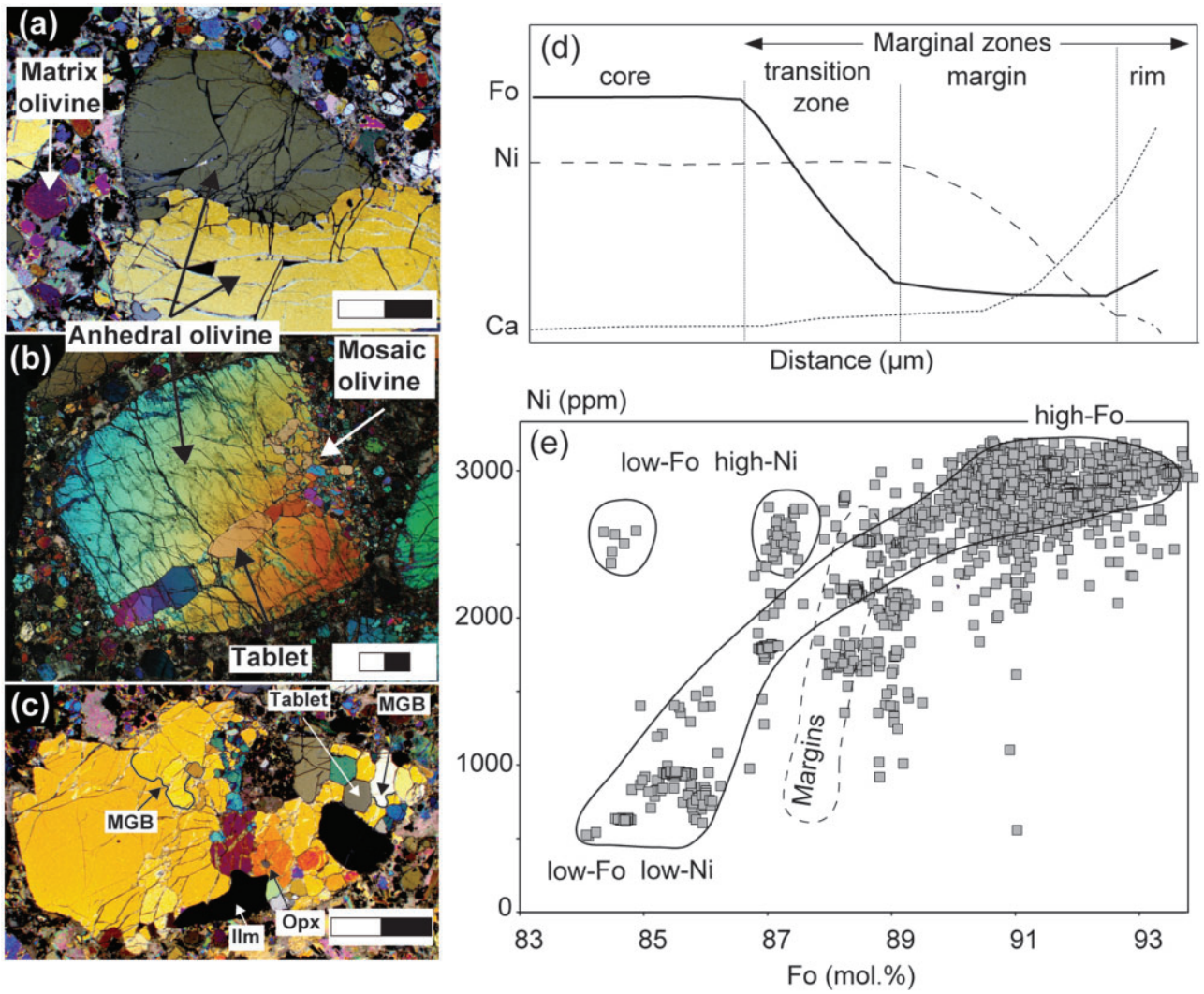

Fig. 1. Olivine nodules in sample NCR27 and olivine composition features in kimberlites. (a) Curvilinear contact between two anhedral olivine grains. (Note the subhedral matrix olivines.) (b) Multigranular nodule with tablets and mosaic-textured grains enclosed in anhedral olivine. (c) Mobile grain boundaries (MGB) in olivine nodule including ilmenite (Ilm) and rounded orthopyroxene (Opx) grains. Scale bar 1 mm. (d) Schematic diagram illustrating the compositional variations in the marginal zones of olivine grains and the terms used in this study to describe the zones. We prefer the terms 'transition zone' and 'rim' to the 'inner margin' and 'edge' of Pilbeam *et al.* (2013). (e) Ni vs Fo content in olivine cores in kimberlites from literature data (Kamenetsky *et al.*, 2008; Brett *et al.*, 2009; Arndt *et al.*, 2010; Pilbeam *et al.*, 2013). Cores with low Ni contents compared with the fields are probably mixed core–margin analyses.

nodule. As seen in Fig. 1e, the Fo content varies from Fo94 to Fo84. At the high-Fo end of this range (Fo>91, 'Type 1 olivines' of Pilbeam *et al.*, 2013) the Ni content is relatively constant and correlates only weakly with Fo content, defining a gentle positive slope in the Fo–Ni diagram. In contrast, at the low-Fo end, the Ni content varies widely to produce two distinct populations, one with low and the other with high Ni contents ('Type 2 and 3 olivines', respectively; Pilbeam *et al.*, 2013).

In the interior of nodules the Fo and minor element contents are remarkably uniform and only in thin and often discontinuous marginal zones does the composition vary significantly (Fig. 1). These marginal zones exhibit the complex compositional variation illustrated schematically in Fig. 1d (Pilbeam *et al.*, 2013). In a complete profile, the core is surrounded by (1) a transition zone (inner margin) in which the Fo content varies but the minor elements such as Ni, Mn and Ca remain almost constant, (2) a margin in which Fo remains almost constant but the minor elements change dramatically, and (3) an outer rim in which both Fo and minor elements vary. Marginal zones can show significant thickness variation within a grain or between grains and are often discontinuous or entirely absent. The variation of the margin thickness results from a combination of processes such as surface area activated growth, with small xenocrystic grains having thinner margins than larger ones (Brett *et al.*, 2009), and subsequent abrasion during upward transport of the kimberlite magma (Jones *et al.*, 2014; Brett *et al.*, 2015).

Even though their Ni and other minor element contents vary considerably, the margins have a restricted range of Fo contents (Fig. 1e). Margin olivine is interpreted to have crystallized directly from the kimberlite liquid, largely because of its enrichment in Ca (Brett *et al.*, 2009; Arndt *et al.*, 2010; Pilbeam *et al.*, 2013). When the Fo content of the core is higher than that of the marginal zones the zoning has been described in the literature as 'normal', and when it is lower the zoning has been said to be 'reverse' (Pilbeam *et al.*, 2013). If additional chemical zones are present, the zoning is 'complex'. These terms may be useful when describing zoned phenocrysts in volcanic rocks in which all zones crystallized from a melt, but we will argue below that the composition range of the cores was produced by a process that was largely independent of the margin crystallization. This being the case, using the terms 'normal', 'reverse' and 'complex' zoning is not appropriate. We will consequently describe the olivine grains based on their core composition, as illustrated in Fig. 1e.

PETROGRAPHY

Samples NCR27 and NCR29 were obtained from a Proterozoic kimberlite dike in the Kangamiut region of West Greenland. Their petrology and chemical composition have been reported by Arndt *et al.* (2006, 2010) and are briefly summarized below. The samples are very well-preserved hypabyssal type-I kimberlite. Sample NCR27 contains 60 vol. % of fresh olivine grains, mostly (~40%) as mono- or multigranular nodules up to 10 mm in size. Sample NCR29 contains far less olivine (25 vol. %), with only 5 vol. % as nodules. Anhedral olivines in the nodules display the high-temperature and high-stress deformation structures typical of nodules and xenoliths in kimberlites, including undulose extinction, close dislocation walls and small subgrains. Xenocrysts of minerals other than olivine are rare and limited to large ilmenite grains (<1 to 2 vol. %), and smaller amounts of phlogopite, serpentinized orthopyroxene, and garnet with kelyphitic rims. Orthopyroxene xenocrysts are rare and occur either dispersed within the matrix or in association with olivine in multigranular nodules. They are systematically rounded (Fig. 1c). The mesostasis is made up of small olivine crystals, phlogopite, Fe–Ti oxides, perovskite, monticellite, apatite and carbonate.

ANALYTICAL METHODS

Major element concentrations in samples NCR27 and NCR29 were measured by inductively coupled plasma atomic emission spectroscopy (ICP-AES) at the University Grenoble Alpes to determine their NiO contents, which were not analysed in the previous study (Arndt *et al.*, 2010). We followed the analytical procedure given by Chauvel *et al.* (2011), using 50 mg of rock powder. The international standard BCR-2 was used for calibration and four other standards (BEN, AGV-1, BHVO-2 and BR-24) were measured as unknown samples to check accuracy and reproducibility. Relative standard deviations are in most cases <1% for SiO_2 and <4% for other major elements.

Back-scattered electron (BSE) images and major and minor element concentrations in olivine were obtained at ISTerre, University Grenoble Alpes (France) using a JEOL JXA-8230 electron microprobe equipped with a single energy-dispersive spectrometer and five wavelength-dispersive spectrometers. Analytical conditions for quantitative analysis of olivine were 25 kV acceleration voltage, 900 nA beam current and electron beam 1 μm in nominal diameter. Raw data reduction was performed using the ZAF procedure. The selected counting time (60 s) allowed us to collect compositional profiles with high spatial resolution (steps of 2–5 μm) and low detection limits (less than 10 ppm for Al, Cr, Ca, Ni and Mn). The San Carlos olivine standard USNM 111312/444 and XEN internal standard were run three times for each 30–50 measurements. Relative standard deviation over 190 measurements is 0·05 wt % for SiO_2, 0·02% for Fo, and less than 0·7% for NiO, Cr_2O_3, CaO and MnO. A few profiles were measured with a longer counting time (720 s), to acquire trace element contents in representative olivine grains (Ti, P, Zn, detection limits lower than 5 ppm). All measurements were corrected for the deviation of the San Carlos standard from the reference values (Jarosewitch *et al.*, 1980). We disregarded analyses

with oxide sums in excess of 100 wt % or cation sums in excess of three, based on four oxygen atoms per formula unit. X-ray element maps were acquired using similar operating conditions (acceleration voltage 25 kV, beam current 900 nA) and dwell times of 100 and 500 ms.

Crystallographic orientations of olivine crystals within multigranular nodules were determined by indexation of electron-backscattered diffraction patterns using facilities at Géosciences Montpellier (CNRS-Université de Montpellier 2, France). Diffraction patterns were generated by interaction of an incident electron beam tilted at 70° with a carefully polished thin section placed in a horizontal holder, in a CamScan Crystal Probe X500 scanning electron microscope. CHANNEL + software (Oxford-HKL Technology) was used for crystallographic orientation indexing and acquisition. The orientation maps of multigranular nodules were obtained in automatic acquisition mode with a step size of 7 μm. Standard post-acquisition data treatment for olivine-rich rocks (Tommasi *et al.*, 2008) allowed the proportion of indexed points to be increased.

RESULTS

Bulk-rock composition

Samples NCR27 and NCR29 were re-analysed to obtain their Ni contents [Supplementary Data (SD) Electronic Appendix Table EA1; supplementary data are available for downloading at http://www.petrology.oxfordjournals.org]. The new analysis of the olivine-poor sample NCR29 is very similar to that reported by Arndt *et al.* (2010). In the nodule-rich sample NCR27, MgO contents are higher (+6 relative %) and Al_2O_3 and CaO are lower (–11·5 and –9 relative %, respectively) than in the previous analyses. However, all the concentrations obtained for NCR27 and NCR29 lie along linear trends in variation diagrams, suggesting that the divergence results from differences in olivine abundance in the analysed aliquots. NiO contents range from 0·10 wt % in NCR29 to 0·18 wt % in NCR27.

Microstructural evidence for grain boundary migration in multigranular nodules

In some multigranular nodules, the contacts between anhedral olivine grains have a distinctive form, being characterized by lobate, concave and convex portions as illustrated in Figs 1c and 2a. We studied the crystallographic orientation of the olivine grains adjacent to such 'bulging' grain boundaries in the multigranular nodule illustrated in Fig. 2. This nodule is 2 mm in diameter and composed of numerous small grains of olivine. Observations under crossed Nicols with an additional lambda plate (Fig. 2a) and a crystallographic orientation map and pole figures (Fig. 2b) demonstrate the presence of five interpenetrating olivine grains with complex shapes and different orientations as shown by their different colours. Two large grains (grains 1 and 2) make up most of the nodule, as shown in Fig. 2c. Misorientation relative to a reference point is less than 15° in these two grains. Bulging grain boundaries are systematically restricted to contacts between grains with different orientation (e.g. between grains 1 and 4, where the misorientation angle is ~20°, Fig. 2a and b).

The shape of the bulging contacts and their location between grains with different crystallographic orientations (Fig. 2b) indicate that these contacts result from grain boundary migration; that is, dynamic, stress-driven recrystallization caused by the difference of internal strain energy stored by dislocations. The migration produces characteristic lobate contacts that separate a concave, dislocation-poor advancing or growing grain from a convex, dislocation-rich retreating or consumed grain (Urai *et al.*, 1986; Drury & Urai, 1990). Such microstructures are described here for the first time in kimberlites; their occurrence provides important constraints on the origin of the nodules and supports the interpretation that they are fragments from deformed lithospheric mantle.

Migrating grain boundaries have been observed in other nodules including both high- and low-Fo types. As seen in Fig. 1c, the olivine tablets crosscut both the mosaic grains and the mobile grain boundaries and therefore postdate these textures.

These observations and interpretations indicate that the following sequence of events affected the olivine in the nodules: (1) generation of a range in olivine compositions; (2) deformation and grain boundary migration; (3) incorporation of dunitic fragments into the ascending kimberlitic magma; (4) growth of olivine tablets.

Core to margin gradients in olivine

The typical core to margin gradients observed in the olivines of sample NCR27 are illustrated by element versus Fo diagrams (Fig. 3) and by a set of chemical profiles (Fig. 4). Chemical analyses are given in SD Electronic Appendix Table EA2.

The margins range in thickness from 30 to 80 μm. They contain numerous fluid inclusions, but are devoid of mineral inclusions. We estimate the volumetric proportion of the margins in sample NCR27 at ~7 vol. % of the total olivine using a false colour image of an FeO microfluorescence map (see Arndt *et al.*, 2010) and ImageJ software (http://rsbweb.nih.gov/ij/).

The margins are characterized by near-constant Fo (Fo87·5 to Fo88·5) contents accompanied by large variations in minor element contents (Fig. 3a–c). In high-Fo grains, Ni contents drop dramatically from 2700 to 580 ppm, whereas Mn, Ca and Ti contents increase (SD Electronic Appendix Table EA2). In low-Fo, low-Ni grains the Fo content is higher in the margins than in the cores, as seen in Figs 3 and 4. In these grains, variations in minor element contents are irregular and not reproducible from one profile to another (Fig. 4c and i). In

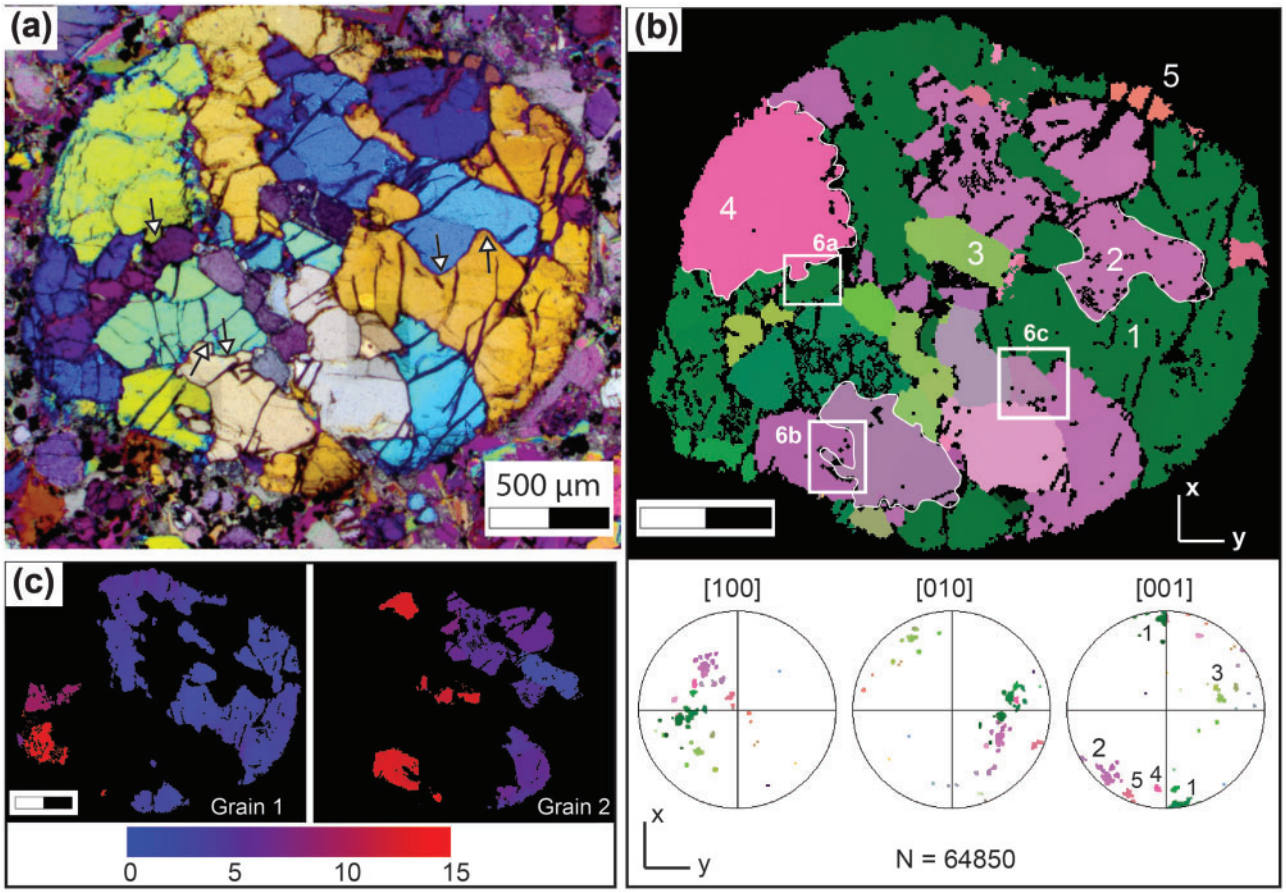

Fig. 2. Crystallographic orientation map of a multigranular nodule in NCR27 determined by electron-backscattered diffraction. (a) Photomicrograph under crossed Nicols with an additional lambda plate. The grains have five orientations corresponding to the different colours (blue, yellow, grey, green, purple). Mobile grain boundaries are arrowed. (b) Orientation map (upper part) and pole figures (lower part). Colours in stereograms (lower hemisphere) are similar to those of the map. N, number of indexed points. Squares show the areas whose compositions have been mapped (Fig. 6). (c) Misorientation maps (0–15°) showing the main two largest grains making up the nodule. Scale bar 500 μm.

particular, the Ni content sometimes increases at the transition between margin and rim (Fig. 4c).

The transition zones between cores and margins vary in thickness from 20 to 60 μm. Within these zones, the Fo content may increase or decrease whereas minor elements remain roughly constant. In high-Fo grains (Fig. 4a), the Fo content decreases sharply and steadily from core to margin. At the same time, Ni content decreases slightly, by less than 100 ppm, and Mn and Ca contents increase slightly, by less than 300 ppm. Transition zones around low-Fo cores are rare and thin (less than 20 μm), and they show a marked increase in Fo whereas Ni remains constant (Fig. 4c).

An important observation is that in minor element versus Fo diagrams (Fig. 3) the transition zones around high-Fo cores coincide with the trends defined by core compositions. For example, in the transition zones in Fig. 4a and b, the NiO content decreases only slightly as the Fo content changes from Fo91 to Fo88·5, reproducing part of the trend defined by high-Fo cores (Fig. 1).

We did not observe the outermost rims (5–10 μm) with extremely Mg-rich composition (Fo96) described from some other well-preserved kimberlites (Kamenetsky *et al.*, 2008; Brett *et al.*, 2009; Pilbeam *et al.*, 2013). However, in some cases, an incipient but sharp increase in Fo content (up to 89·5) associated with a small decrease in Ni (up to 500 ppm) and increase in Ca and Mn (up to 6000 ppm and 3000 ppm, respectively) is observed at the crystal edge (Fig. 4c and g).

Mobile grain boundaries and grain boundary zones

In sharp contrast to the remarkably uniform compositions in the interiors of most nodules, a few exceptional multigranular nodules, such as those illustrated in Figs 2 and 5, show large internal variations in Fo content. For example, the nodule in Fig. 5b contains numerous irregular zones adjacent to internal grain boundaries in which the Fo content is far lower than that of the core olivine. The distinctive features of these zones, which we will call 'grain boundary zones', are as follows: (1) they are adjacent to lobate (i.e. mobile) grain boundaries (Fig. 5); (2) the chemical gradients on opposing sides of the mobile grain boundaries are asymmetric, wide in the concave (growing) grain (up to

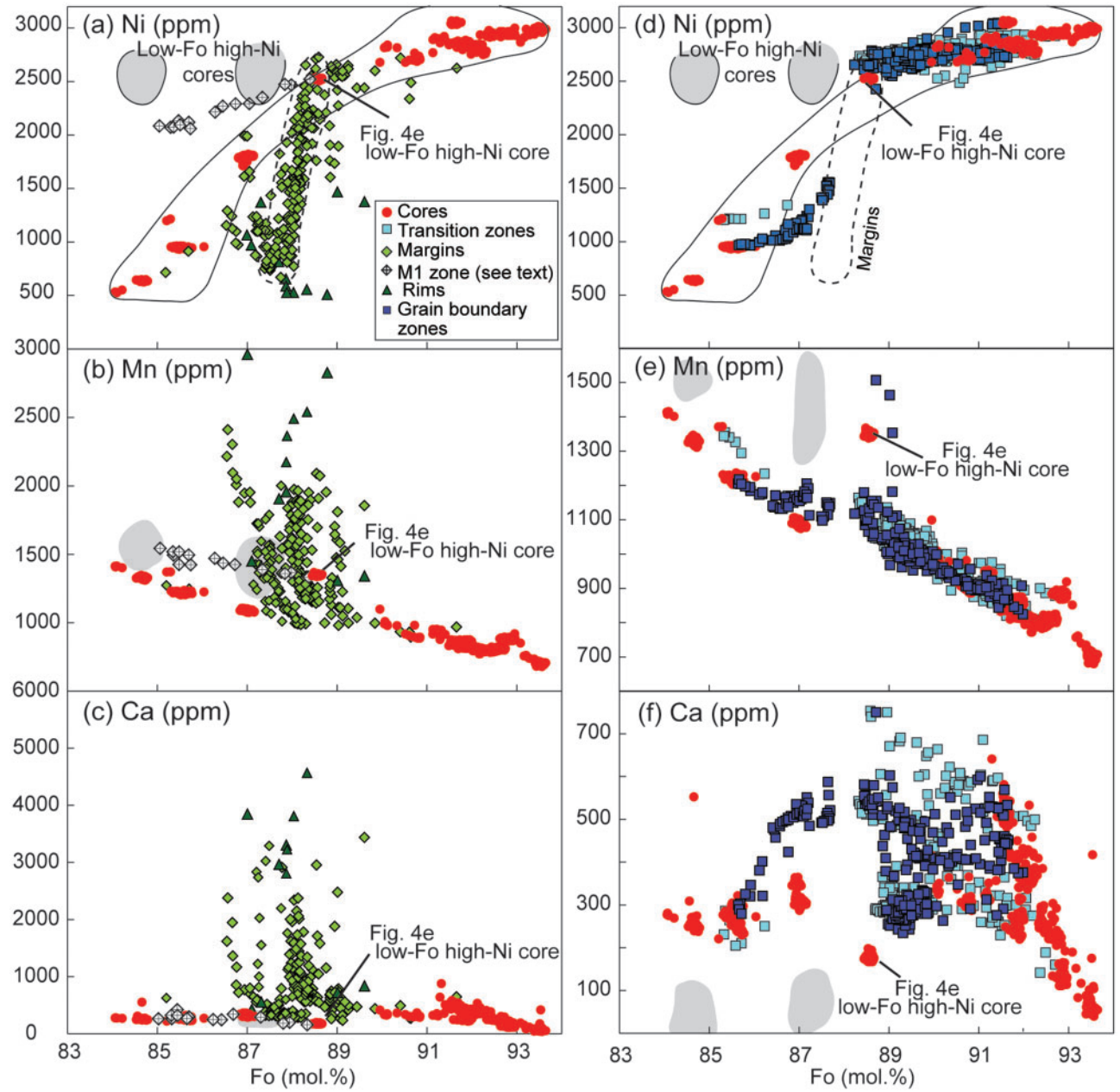

Fig. 3. Minor element (Ni, Mn, Ca) vs Fo variations. (a–c) Cores and margins; (d–f) cores, grain boundary zones and transition zones. Fields for low-Fo, high-Ni cores are after Pilbeam *et al.* (2013).

60 μm thick) but absent or very thin in the convex (consumed) grain; (3) the variations in Fo and minor elements are decoupled in the same way as in transition zones. The Fo content changes from uniform in the core to more variable in the grain boundary zone, whereas minor elements remain roughly constant and similar to those of the core.

In the high-Fo nodule in which we measured crystallographic orientations (Fig. 2), the Fo content of the growing grain decreases within the grain boundary zone from Fo92·7 (the core value) to Fo89, whereas minor elements remain constant (Figs 6 and 7a–d). Outwards, a zone with constant Fo and variable minor elements, like that observed in margins, lines the mobile grain boundary. Most notably, the Ca content increases dramatically, up to 3000 ppm (Fig. 7a). In the convex consumed grain, the core-to-margin transition is abrupt and marked by sharp jumps in Fo and minor element contents.

In the light of the above observations, we re-examine the intra-grain variations of the olivine composition in the large high-Fo (Fo93) multigranular nodule shown in Fig. 5b. This nodule is distinguished by numerous, large grain boundary zones, each of which displays distinctive chemical compositions and gradients. In chemical maps (Fig. 8), three zones with low Fo contents (Fo89) are seen to penetrate the high-Fo olivine cores. Minor elements are similar in the low-Fo zones and cores. The

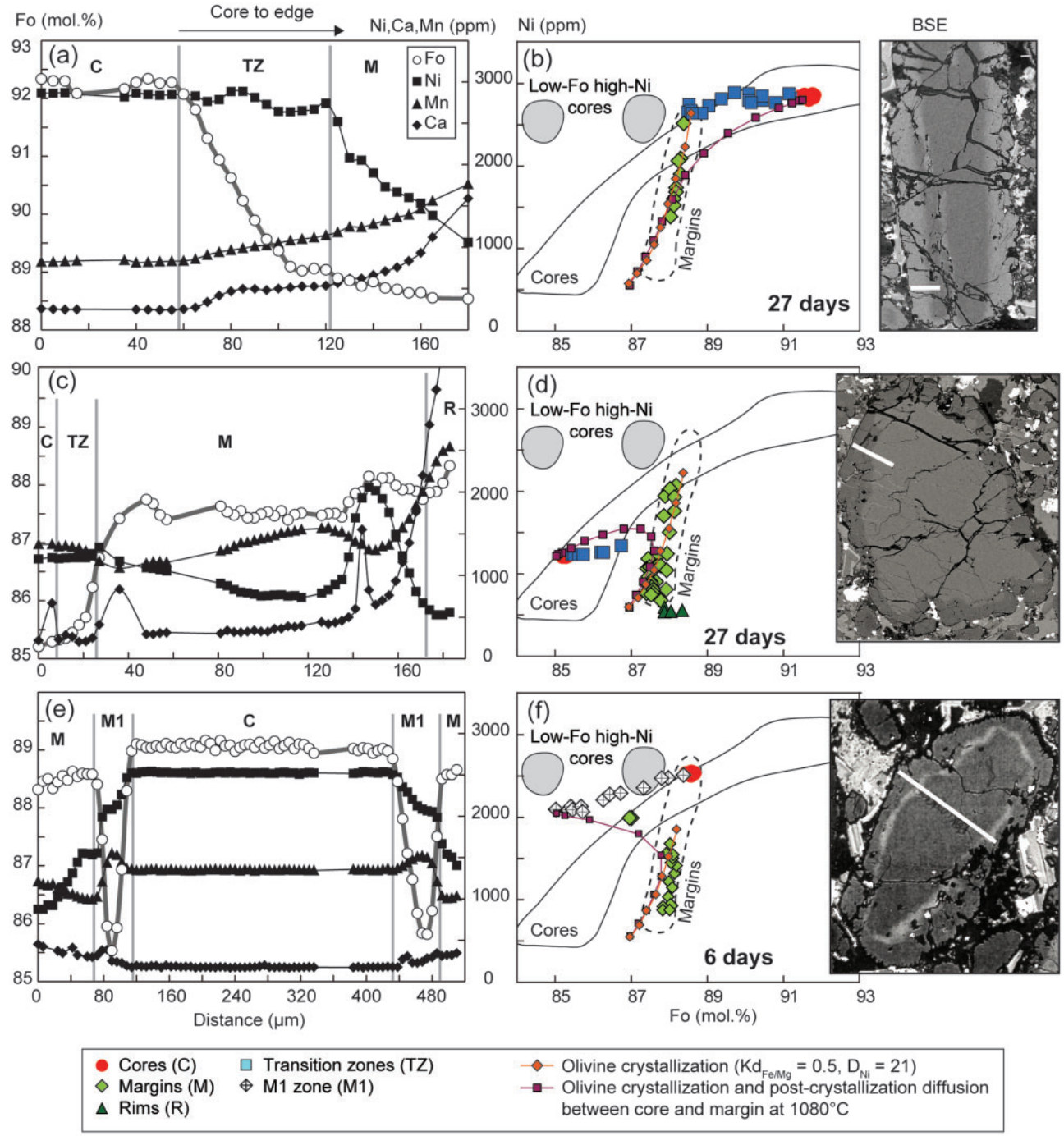

Fig. 4. Chemical profiles across marginal zones in olivine grains (a, c, e, g, i, k) and position of the data in Ni vs Fo diagrams (b, d, f, h, j, l). Position of the profiles is indicated on the back-scattered (BSE) electron images. Results of calculations for crystallization of olivine margin and post-crystallization diffusion between cores and margins during the indicated time intervals are shown in the right-hand panels.

(continued)

low-Fo zones are delimited on one side by lobate grain boundaries, which are marked by a sharp decrease in Fo and Ni contents and an increase in elements incompatible in olivine (Mn, Ca, Ti, Fig. 8). On the other side, the Fo content progressively increases to attain the high-Fo core composition, whereas the Ni content remains relatively constant. The lobate shape of internal grain boundaries, the asymmetric distribution of the low-Fo zones across the grain boundaries and their distinctive chemical gradients are characteristics of grain boundary zones.

Migrating grain boundaries and grain boundary zones are also identified in the low-Fo nodule illustrated in Fig. 7e and f. Mobile grain boundaries coexist with tablets and mosaic-textured grains but variations in olivine composition are restricted to the mobile grain

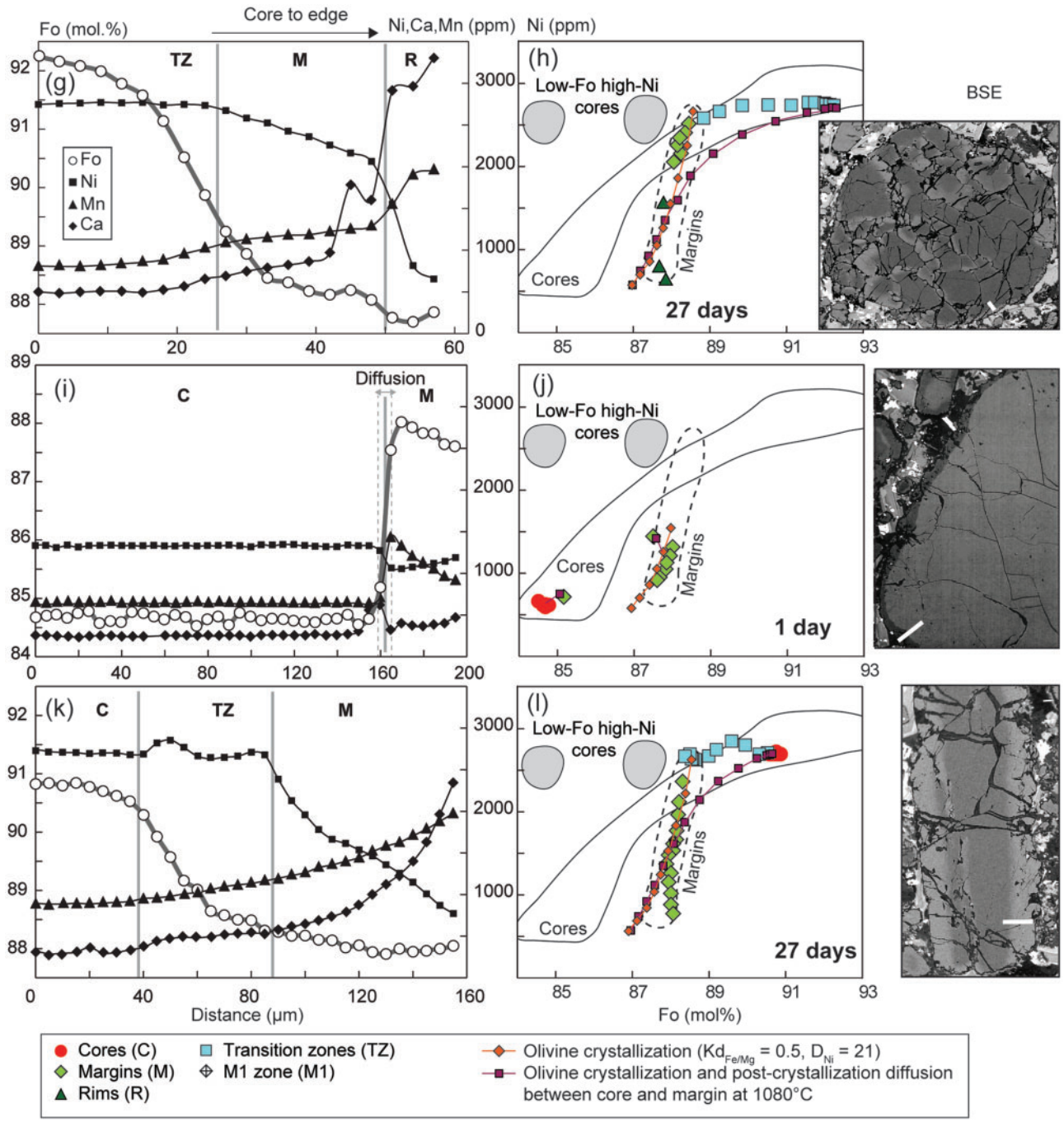

Fig. 4. Continued

boundaries. The grain boundary zone is asymmetric and marked by an increase of the Fo content in the bulging grain. The Ni content, like that of other minor elements, increases only slightly (Fig. 7e). In a Ni versus Fo diagram, the composition of the grain boundary zone lies on curving trends linking low-Fo core composition to the composition of the margin itself (Figs 5 and 7f).

KIMBERLITE MELT COMPOSITION

The composition of the kimberlite melt cannot be estimated directly from the bulk composition of sample NCR27 because of the high amount of xenocrystic olivine and the presence of large but rare ilmenite megacrysts (*c.* 60 vol. % olivine and 40 vol. % nodules; Arndt *et al.*, 2006). However, we can infer the parental melt composition from the chemical composition of NCR27 and that of another sample of the same dike (NCR29), which contains far less olivine (25 vol. % with 5 vol. % nodules; Arndt *et al.*, 2006). Two different values for the Fe–Mg distribution coefficient between olivine and melt ($Kd_{Fe–Mg}$) have been discussed in the literature (Kamenetsky *et al.*, 2008; Arndt *et al.*, 2010; Pilbeam *et al.*, 2013). A $Kd_{Fe–Mg}$ value of 0·3 is normally adopted

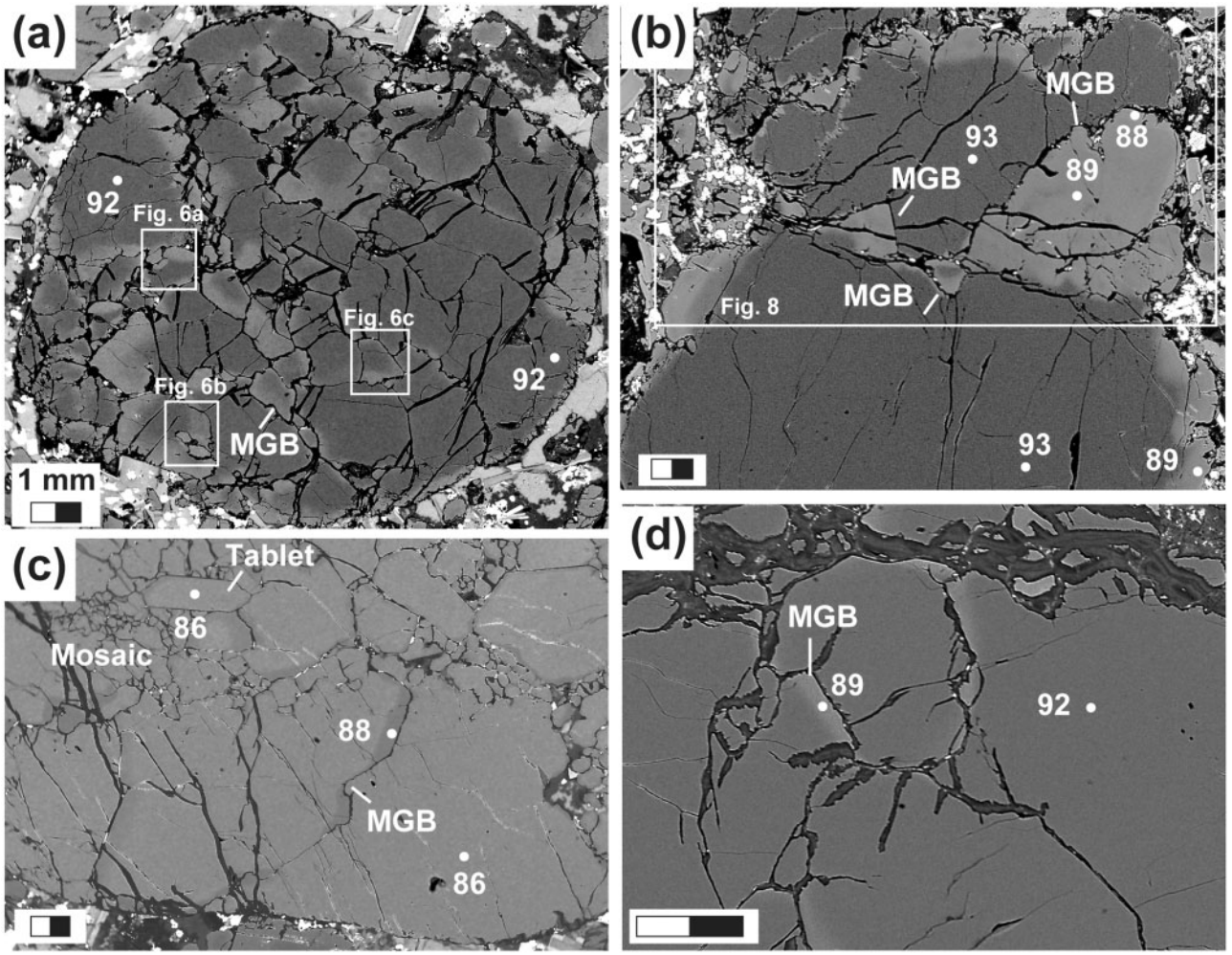

Fig. 5. Back-scattered electron images of mobile grain boundaries (MGB) in four nodules from sample NCR27. Light grey indicates Fo-poor compositions. Fo content (mol %) in olivine is indicated. Squares show the areas in which the compositions have been mapped (Figs 6 and 8). Scale bar in (b), (c) and (d) 200 μm.

for basaltic melts (Roeder & Emslie, 1970), whereas a value of 0·5 has been proposed for CO_2-rich kimberlite melts (Dalton & Wood, 1993; Girnis *et al.*, 2005). All iron can be considered to be FeO because of the reduced state of kimberlite magmas (ΔNNO = –3 to –2, where NNO is nickel–nickel oxide; Fedortchouk & Canil, 2004).

The MgO content of the parental melt can be determined graphically in an FeO versus MgO diagram (Fig. 9). The values are MgO = 20 wt % for $Kd_{Fe–Mg}$ of 0·3 and 30 wt % for $Kd_{Fe–Mg}$ of 0·5. These MgO values can then be used to estimate the concentrations of the other major and minor elements in the parental melt (Table 2) using trends between NCR27 and NCR29 samples in element versus MgO diagrams. For both $Kd_{Fe–Mg}$ values, the calculated parental melts have magnesium-rich silicocarbonatite composition (SiO_2 = 30–32 wt %, MgO = 20–30 wt % and FeO = 14–15 wt %, normalized to 100 wt %, without volatiles, Table 2). The new analyses allow us to determine the Ni contents: 120 ppm for the 30 wt % MgO melt and 770 ppm for the 20 wt % MgO melt.

To reproduce the compositions of the NCR29 and NCR27 samples, which both contain xenocrystic olivine, we added olivine (+ ilmenite) to the parental melt composition (Fig. 9; Table 2). The xenocryst assemblage is dominated by olivine (94 wt %), with a bulk Fe–Mg value very close to the average composition of all xenocryst cores analysed in NCR27 (Fig. 9). A small amount of xenocrystic ilmenite is required to account for the high TiO_2 content of NCR27. Calculated xenocryst versus melt proportions change depending on the $Kd_{Fe–Mg}$ value (Table 2). The xenocryst proportions obtained using a value of 0·3 (53 vol. % in NCR27 and 29 vol. % in NCR29) agree well with the amount of olivine (nodule + matrix olivine) observed in thin section (60 vol. % in NCR27 and 25 vol. % NCR29; Arndt *et al.*, 2010). Previous studies of the chemical and microstructural characteristics of matrix olivine grains have shown that a large proportion of these grains is xenocrystic (Brett *et al.*, 2009; Arndt *et al.*, 2010), supporting the view that the kimberlite melt is in equilibrium with olivine with a $Kd_{Fe–Mg}$ value of 0·3.

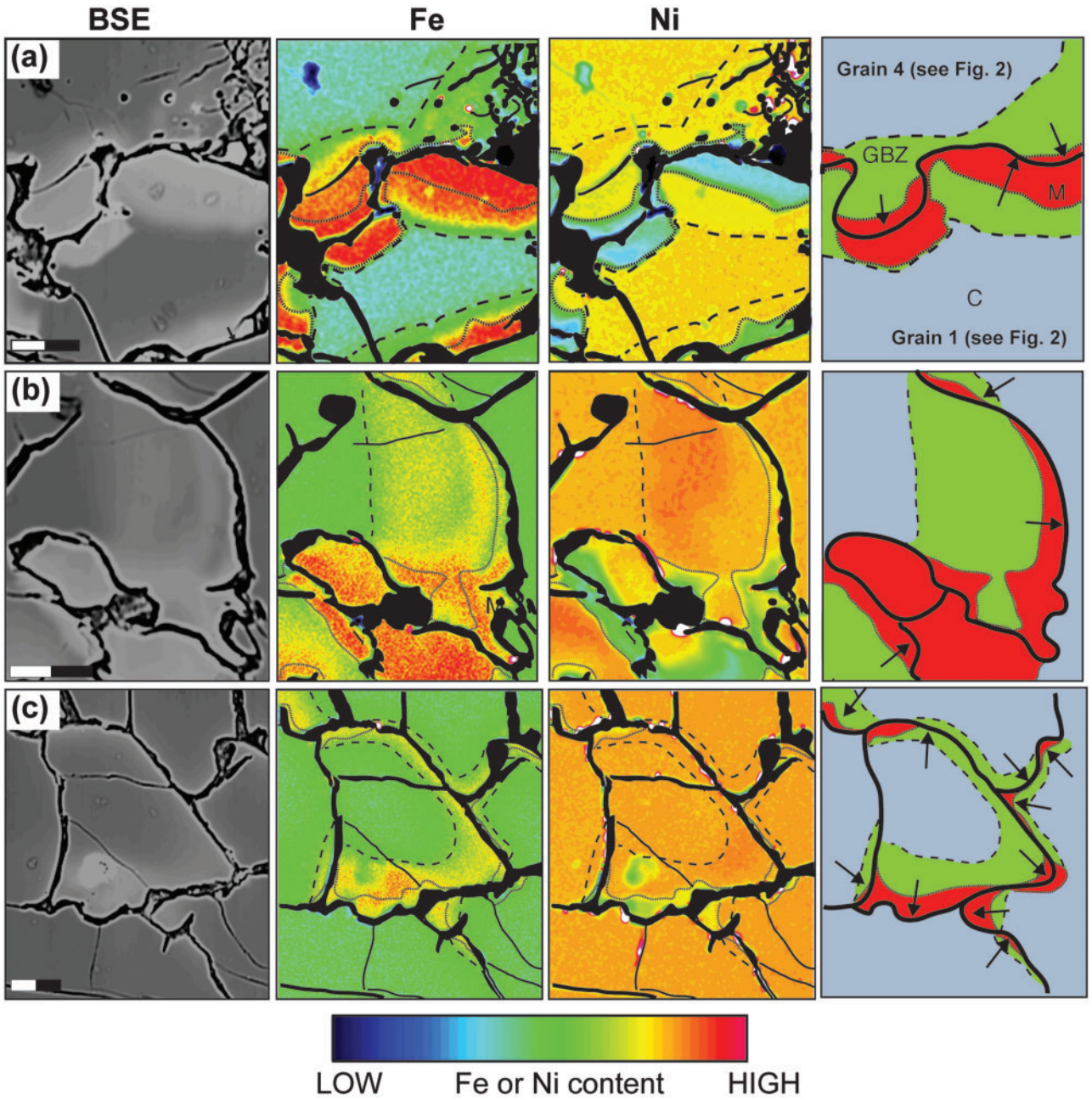

Fig. 6. Back-scattered electron (BSE) images and Fe and Ni distribution maps of the grain boundary zones (GBZ) in the multigranular nodule shown in Figs 2 and 5a. Scale bar 50 μm. Sketches (right) indicate the distribution of the core (blue), margin (red) and grain boundary zone (green) across the mobile grain boundary. The direction of migration is arrowed. The variation of thickness of the grain boundary zone between grown and consumed grains and in a single grain should be noted.

OLIVINE COMPOSITION: CRYSTALLIZATION VERSUS MELT REACTION

Is digestion of orthopyroxene coupled to margin crystallization?

The olivine margins that crystallized from the kimberlite melt have near-constant Fo contents (~Fo88) but variable minor element contents, most notably showing a dramatic decrease in Ni (Fig. 3a). The buffering of the Fo content in cognate olivine has been attributed by Kamenetsky *et al.* (2008) and Arndt *et al.* (2010) to a higher $Kd_{Fe/Mg}$ value than usually assumed for basaltic melts, and by Pilbeam *et al.* (2013) to concomitant crystallization of olivine and assimilation of orthopyroxene ('digestion fractional crystallization'). To test these possibilities we modelled the variations of olivine composition using incremental mass-balance calculations based on the two kimberlite-like parental melts listed in Table 2 and on a low-silica carbonatitic liquid (Pilbeam *et al.*, 2013).

We found no evidence of co-crystallization of high-Ni phases such as spinel, ilmenite or sulfide during margin crystallization. Cognate margins are typically devoid of

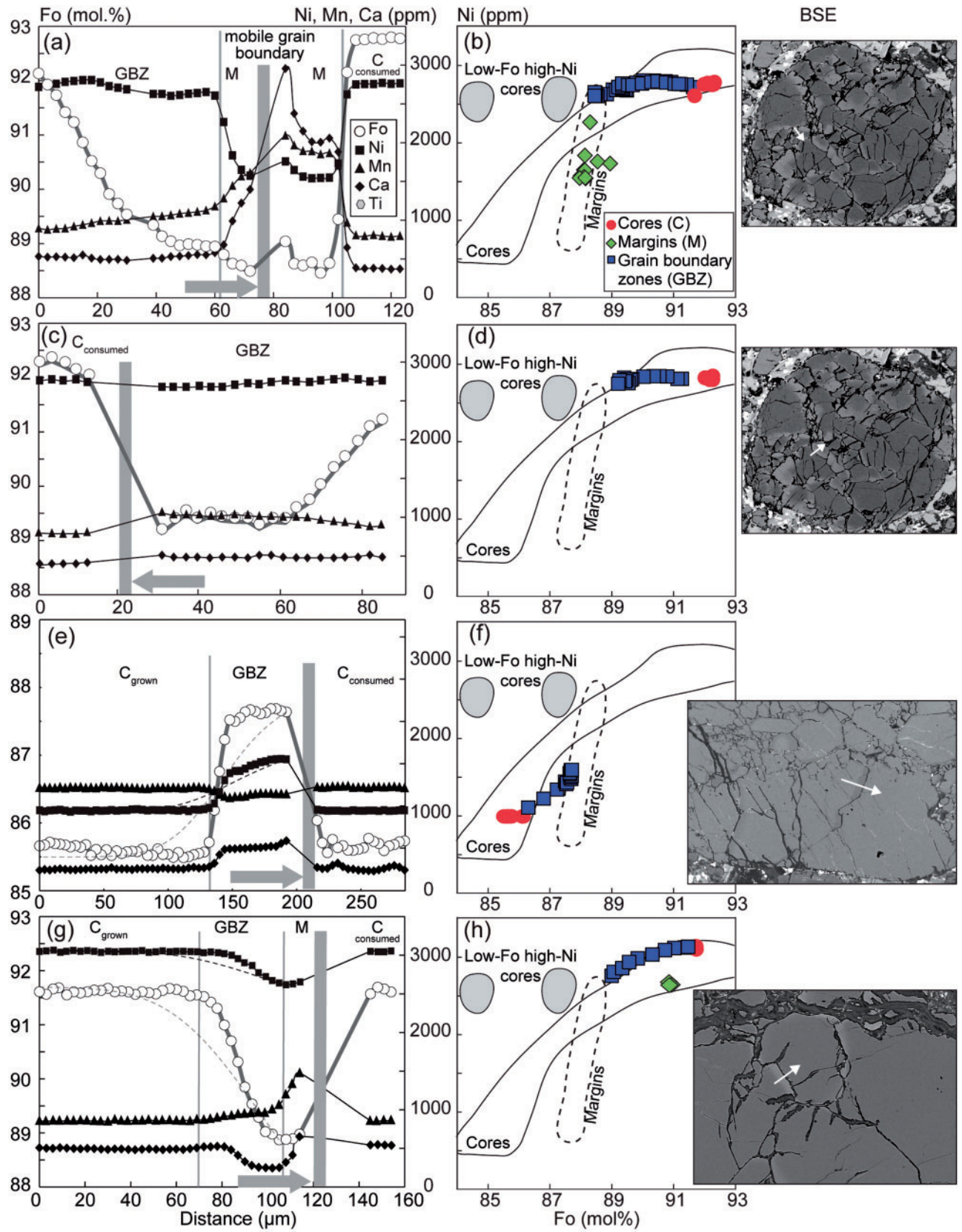

Fig. 7. Chemical profiles (a, c, e, g) across mobile grain boundaries and position of the analyses (b, d, f, h) in a Ni vs Fo diagram. The position of the profiles is indicated on the BSE images. Direction of migration is shown on the profiles by the grey arrows. Results of calculations for diffusive equilibration over 3 days between core and grain boundary zone at mantle temperature (1400°C) and pressure (1 GPa) are shown in (e) and (g) for Fo (grey dashed line) and Ni (black dashed line).

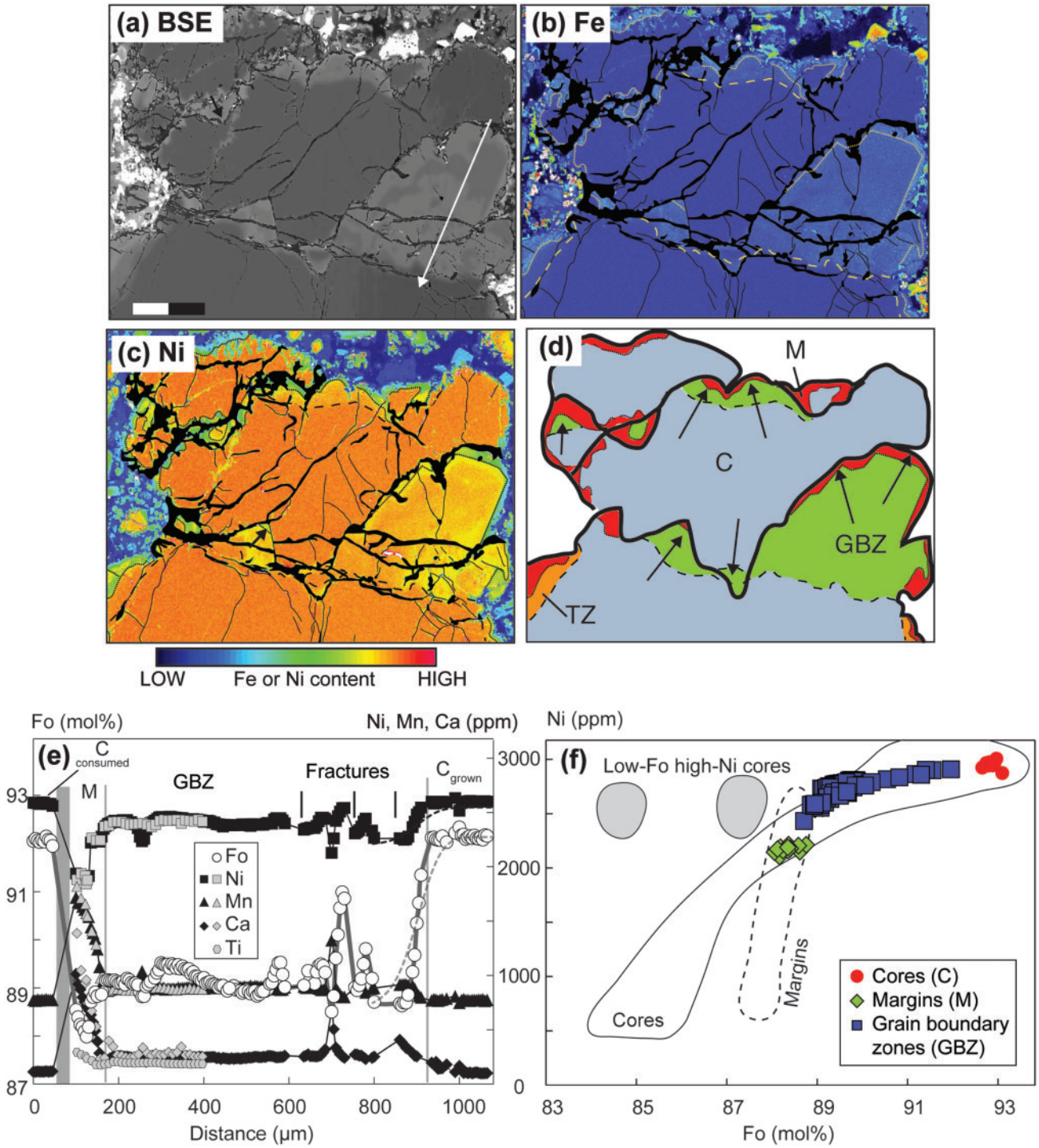

Fig. 8. Grain boundary zones (GBZ) in the multigranular nodule shown in Fig. 5b. (a–d) BSE images and Fe and Ni distribution maps. Scale bar 400 μm. Sketch in (d) indicates the distribution of the core (C, blue), margin (M, red), grain boundary zone (GBZ, green) and transition zone (TZ, orange). The direction of migration is arrowed. (e, f) Chemical profile along the transect shown in (a) and position of the analyses in the Ni vs Fo diagram. Minor elements plus Ti were analyzed using a high-resolution procedure (see text), as shown on the left side of the profile (grey symbols). Results of calculations for diffusive equilibration over 7 days between core and grain boundary zone at mantle temperature (1400°C) and pressure (1 GPa) are shown in (e) for Fo (grey dashed line) and Ni (black dashed line).

oxide inclusions and, when measured, the TiO_2 content increases within the margins (Fig. 8e), precluding ilmenite co-crystallization. We thus assumed that olivine was the only phase to crystallize. Assimilation of orthopyroxene coupled to fractional crystallization of olivine was modelled using the formulation of DePaolo (1981) and the parameters given in Table 3. Orthopyroxene has the highest potential to contaminate

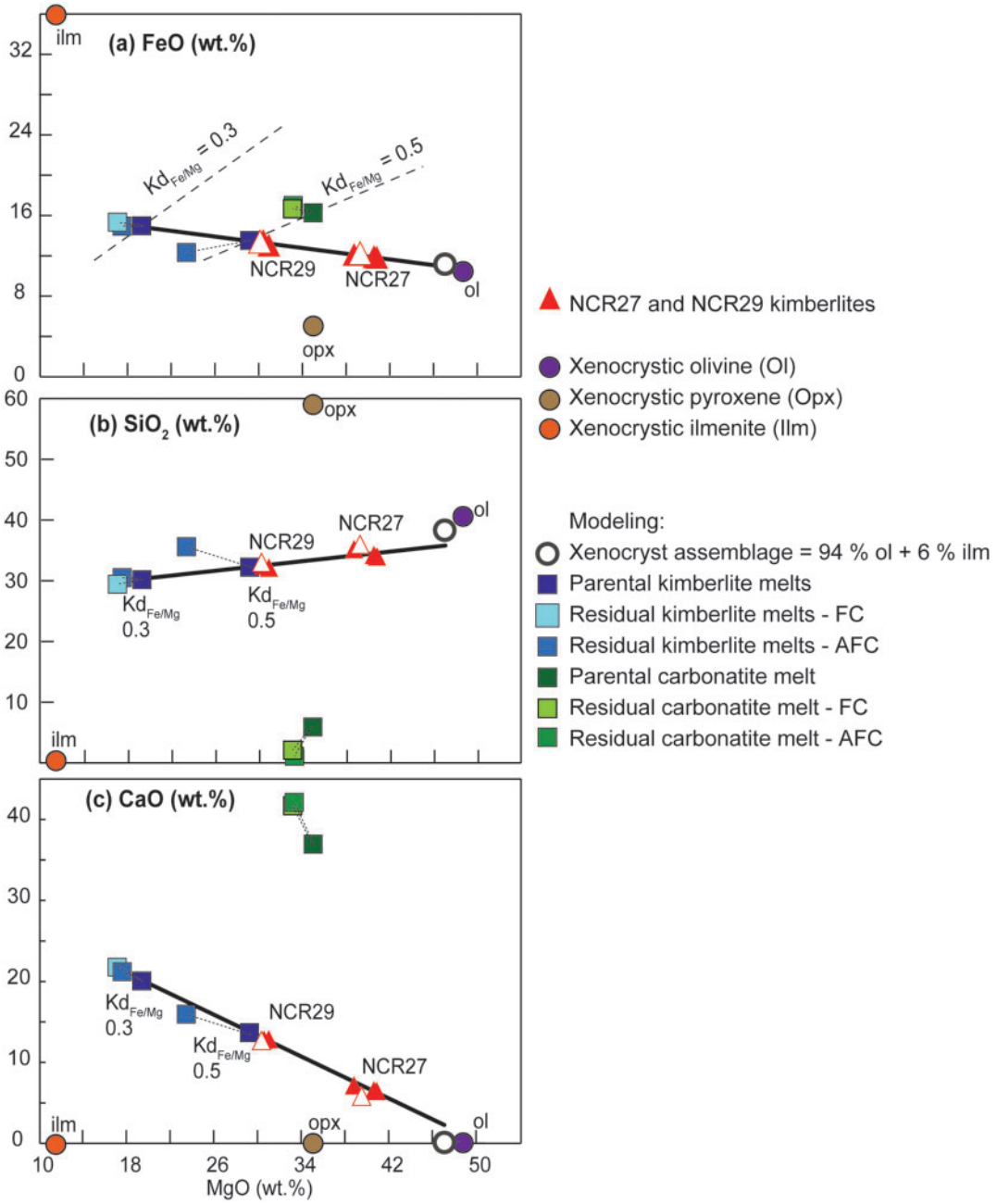

Fig. 9. Variation of FeO (a), SiO_2 (b) and CaO (c) vs MgO (wt %) in NCR27 and NCR29 kimberlite samples (40 and 5 vol. % olivine nodules, respectively) and in computed parental and residual melts. The xenocrystic line (bold line) connects the nodule-rich NCR27 sample and the nodule-poor NRC29 sample and shows the effect of addition of the xenocryst assemblage (94% olivine + 6% ilmenite). The composition of the xenocrystic olivine is the average of the analyzed core compositions; the compositions of xenocrystic ilmenite and orthopyroxene are from Nielsen & Sand (2008). The $Kd_{Fe/Mg}$ sloping dashed lines in (a) represent the FeO/MgO ratio of melts in equilibrium with olivine margin composition considering $Kd_{Fe/Mg}$ values of 0·3 and 0·5. The intersection of the $Kd_{Fe/Mg}$ lines and the xenocrystic line gives the MgO and FeO contents of the parental kimberlite melt (Table 2). The proportion of xenocrysts in NCR27 and NCR29 is back-calculated from the composition of the parental melts, xenocryst assemblage and kimberlite samples. The carbonatite-like parental melt composition is from Pilbeam *et al.* (2013). The dotted line connects the parental melts and the residual melts obtained by fractional crystallization of olivine (FC) and by orthopyroxene assimilation coupled with fractional crystallization (AFC). (See text and Table 3 for further details.)

the kimberlite melt because the reactivity of mantle minerals with a low-silica melt decreases from orthopyroxene to clinopyroxene to olivine (Luth, 2009; Russell *et al.*, 2012).

In mafic and ultramafic magmas the partition coefficient of Ni in olivine (D_{Ni}) depends on melt composition, in particular the MgO content (e.g. Hart & Davies, 1978; Li *et al.*, 2001). The compositional dependence of D_{Ni} in alkali-rich carbonatite melts with variable MgO contents has not been investigated experimentally, but we assumed that D_{Ni} is negatively correlated with the MgO content of the melt (Table 3). The D_{Ni} values were

Table 2: Volatile-free major element composition (wt %) of the kimberlite, carbonatitic and basaltic parental melts considered for the modeling of margin crystallization

	SiO_2 (wt %)	TiO_2 (wt %)	Al_2O_3 (wt %)	FeO^T (wt %)	MnO (wt %)	MgO (wt %)	CaO (wt %)	Ni (ppm)	vol. %* NCR27	vol. %* NCR29
Kimberlite[†]										
Ol $Kd_{Fe/Mg} = 0{\cdot}5$	32·2	3·4	3·4	13·5	0·3	29·2	13·7	767	40	5
Ol $Kd_{Fe/Mg} = 0{\cdot}3$	30·2	3·2	5·4	14·9	0·3	19·4	20·0	130	53	29
Carbonatite[‡]	5·9	2·2	0·6	16·2	0·18	35·0	37·0	208		
Basalt	48·7	1·1	15·1	9·6	0·2	10·6	12·8	280		

*Proportions of xenocryst assemblage (94% olivine plus 6% ilmenite) that have to be added to the melt to reproduce the compositions of NCR27 and NCR29. Proportions are converted to vol. % using densities of 3200, 4720 and 2450 kg m^{-3} for olivine, ilmenite and kimberlite melts, respectively.

[†]Kimberlite parental melt determined from Fig. 9 (see text).

[‡]Carbonatite parental melt from Pilbeam *et al.* (2013).

Table 3: Parameters used in crystallization models

Parental melt*	Kimberlite	Kimberlite	Carbonatite	Basalt
Fe^{2+}/Fe^{tot}	1	1	1	0·85
Ol $Kd_{Fe/Mg}$	0·5	0·3	0·5	0·3[†]
Cpx $Kd_{Fe/Mg}$	–	–	–	0·27[†]
Ol D_{Ni}[‡]	4	21	13	7–12
f[‡]	105	400	450	–
Cpx D_{Ni}	–	–	–	1
FC	–	ol	ol	ol + cpx
Cum. %[§]	–	9	14	16
Ni in ol (ppm)	–	575	575	2045
Fo in ol	–	86·9	87·5	84·7
AFC	ol–opx	ol–opx	ol–opx	–
Cum. %[§]	37	10	15	–
Opx %[§]	22	4	3	–
r[§]	0·6	0·4	0·2	–
Ni in ol (ppm)	800	535	513	–
Fo in ol	87·2	87·4	87·7	–

*Parental melt compositions are given in Table 2.

[†]$Kd_{Fe/Mg}$ values from Roeder & Emslie (1970) and Irving (1984).

[‡]Partition coefficients for Ni in olivine. In kimberlite and carbonatite melts, $D_{Ni} = f$/MgO. In basaltic melt, ln $D_{Ni} = 5{\cdot}67–1{\cdot}38$ ln MgO – 0·25 (FeO/MgO) (Li *et al.*, 2001).

[§]Cum. %, weight per cent of crystallized cumulate; opx %, weight per cent of assimilated opx; r, ratio of assimilation rate to crystallization rate (DePaolo, 1981).

evaluated from equilibrium between the parental melts and the margins with the highest Ni content. D_{Ni} varies depending on the $Kd_{Fe/Mg}$ used for the parental melt calculation, with D_{Ni} values ranging from three for $Kd_{Fe/Mg} = 0{\cdot}5$ to 21 for $Kd_{Fe/Mg} = 0{\cdot}3$ (Table 3). A combination of high $Kd_{Fe/Mg}$ with high D_{Ni} does not reproduce the chemical variations observed in olivine margins when kimberlite-like melts are considered (Table 3).

The D_{Ni} values are well above the range proposed for basaltic melts (e.g. 3·8–5 at 1400–1550°C; Matzen *et al.*, 2013) but are realistic in view of the following characteristics of kimberlite melts: (1) they are rich in carbonate and D_{Ni} up to 19 has been proposed for silicocarbonatite melts (Sweeney *et al.*, 1995; Girnis *et al.*, 2013); (2) they are rich in potassium ($K_2O \sim Al_2O_3$; SD Electronic Appendix Table EA1) and a D_{Ni} up to 40 has been proposed for highly potassic rocks (Foley *et al.*, 2011); (3) they crystallized at lower temperatures (1080–1170°C; Fedortchouk & Canil, 2004) than basaltic melts and D_{Ni} increases with decreasing temperature, at least in basaltic systems (Matzen *et al.*, 2013).

The modelled chemical trends are compared with margin compositions in Ni versus Fo diagrams (Figs 4 and 10). We used the composition of the two kimberlite samples with different xenocryst proportions to check that the modelled residual melts plot on similar trends to the bulk-rocks and xenocrystic assemblage in major element versus MgO diagrams (Fig. 9). Models considering a carbonatitic parental melt succeed in reproducing the margin olivine composition but the residual melts have too low SiO_2 and too high CaO to explain the compositions of the NCR27 and NCR29 samples by olivine (+ ilmenite) addition.

Both crystallization models based on parental kimberlite melts give residual melts consistent with the bulk compositional trends, but the cognate olivine compositions are different. The model with high $Kd_{Fe/Mg}$ and low D_{Ni} (Table 3) reproduces the buffering of Fo content only if orthopyroxene is simultaneously assimilated. However, unrealistically high proportions of crystallized olivine (37 wt %) and assimilated orthopyroxene (22 wt %, Table 3) are needed to reproduce the low Ni contents at the end of the trends. The proportion of margin olivine is only 7 vol. % (~6 wt %) in NCR27 and only 4 wt % in other kimberlite samples (e.g. Brett *et al.*, 2009). Reconciling model and observation would require the presence of a large amount of cognate olivine in the kimberlite matrix, which is inconsistent with the low observed proportion of phenocrysts (less than 1 vol. %, Brett *et al.*, 2009).

If a low $Kd_{Fe/Mg}$ and high D_{Ni} are adopted, however, the required amount of olivine crystallization is low (8–9 wt %, Table 3) and consistent with the proportion of olivine margins. The cognate olivine composition can be reproduced considering fractional crystallization of olivine only (Fig. 10) or olivine crystallization accompanied by the assimilation of a negligible amount of orthopyroxene (<5 wt %, Table 3).

Olivine crystallization from basaltic melt

A single complexly zoned grain in the matrix contains an unusual M1 zone between core and margin,

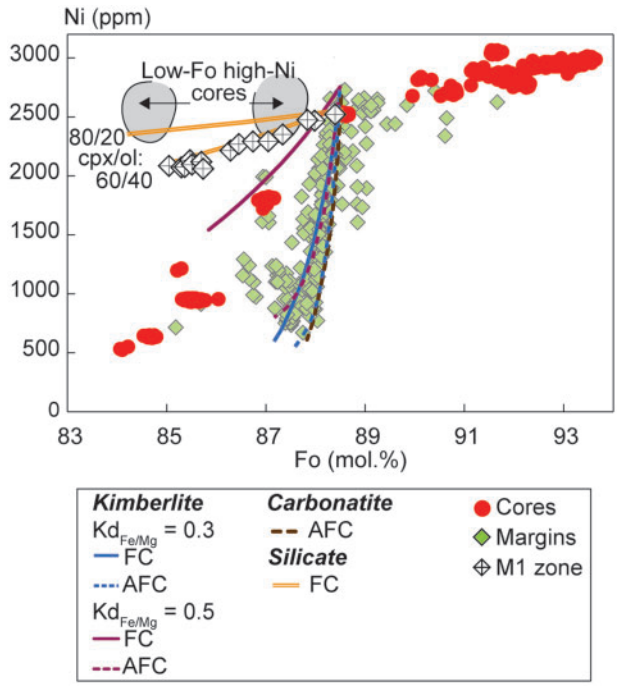

Fig. 10. Ni vs Fo diagram showing the margin crystallization models summarized in Table 3. For crystallization of the silicate melt, two trends are drawn for two ratios of crystallizing clinopyroxene and olivine.

characterized by low Fo contents but high Ni and Mn contents (Figs 4e, f and 10). In contrast to the other marginal zones, in which Ni contents drop rapidly, in this zone the Ni content decreases only from 2500 to 2100 ppm as the Fo content decreases from 89·2 to 85·5. The latter value is lower than any other values in zoned olivine grains, except for the low-Fo high-Ni population (Type 3 olivine) identified by Pilbeam *et al.* (2013). We attribute this trend to crystallization of olivine from a basaltic (Tables 2 and 3), rather than an ultramafic melt. At high pressure clinopyroxene crystallizes together with olivine and because the Ni partition coefficient in clinopyroxene is lower (e.g. $D_{Ni} = 2{\cdot}8$; Laubier *et al.*, 2014) than that for olivine, co-precipitation of the two phases results in only a subdued drop in the Ni content of the residual liquid. We could obtain a fit with the M1 zone composition considering a partition coefficient in clinopyroxene of unity (see Table 3 and Fig. 10). This value is slightly lower than those proposed for basaltic systems at atmospheric pressure (e.g. 2·8, Laubier *et al.*, 2014), but by comparison with the partitioning of Ni in olivine, the value must be lower at high mantle temperature and pressure (e.g. Matzen *et al.*, 2013). The M1 zone also has low Ca contents (Fig. 3c), a feature consistent with co-crystallization of calcic clinopyroxene. The core of the complexly zoned grain shares the low Fo, high Ni, high Mn and low Ca contents of the M1 zone that surrounds it. In this sense, it differs radically from the other olivine cores in the NCR27 sample, but it is similar to the rare (<1 vol. %) Type 3 low-Fo high-Ni cores reported by Pilbeam *et al.* (2013) in other Greenland kimberlites (Fig. 3). This may indicate that both the core and the M1 zone crystallized from a basaltic melt. The M1 zone is mantled outward by typical margins, suggesting that the crystallization of basaltic melt preceded kimberlite crystallization. If this interpretation is correct, we have evidence that kimberlite magmas interacted with deep-seated basalts in the lithosphere, before crystallization of the margin from the kimberlite melt.

Do transition zones result from diffusive equilibration?

Pilbeam *et al.* (2013) attributed the transition zones to diffusive equilibration after crystallization of the margins. Two observations oppose this interpretation: (1) the Fo content in the transition zones varies significantly from core to margin composition whereas Ni remains constant and similar to the core composition; (2) the evolution from transition zone to margin is sharp with the preservation of abrupt changes in minor element contents, notably Ni.

The continuous change of the Fo content in the transition zones would require a high degree of diffusive equilibration, if produced by this process. Like Pilbeam *et al.* (2013), we calculated a duration of equilibration of 1 month for a 60 μm thick transition zone (Fig. 4), using the parameterization of Dohmen & Chakraborty (2007) for the Fe–Mg inter-diffusion coefficient along the [001] crystallographic axis at atmospheric pressure and 1080°C (Fedortchouk & Canil, 2004). The diffusion time is reduced to 10 days if a higher crystallization temperature is considered (1170°C, Fedortchouk & Canil, 2004), but this duration is still significantly longer than the total ascent time of the kimberlite magma to the surface (less than 10 h; Canil & Fedortchouk, 1999; Wilson & Head, 2007; Russell *et al.*, 2012).

Given that Ni and the Fe–Mg pair have similar diffusion rates (Petry *et al.*, 2004), during the time required to produce continuous variations of Fo through the transition zones, Ni would also have diffused, producing correlated variations of Ni and Fo in the transition zones; such variations are not observed in the nodules (Fig. 4).

Some post-crystallization diffusion no doubt occurred but we believe that the effects on olivine are limited. One example can be seen in Fig. 4i and j. In this low-Fo low-Ni grain, a transition zone is absent and core and margin are in sharp contact. Any diffusion was limited to less than 10 μm at the boundary between core and margin (Fig. 4i). In the Fo versus Ni diagram (Fig. 4j), diffusion may have produced the observed minor deviations from core and margin compositions but certainly does not create the continuous chemical trend observed in the transition zones.

To summarize, post-crystallization diffusion between cores and margins cannot explain the 60 μm thick transition zones with the continuous variation in Fo content, the lack of equilibration between transition zones and margins, and the characteristic decoupling between Fo

and minor elements. This suggests that transition zones record a magmatic process that modified the olivine composition at the nodule and grain borders, before crystallization of the margins.

Grain boundary zones: grain-scale fluid percolation

In this section, we examine the chemical variations across mobile grain boundaries, and explore how they shed light on the origin of the grain boundary zones and what this tells us about the origin of olivine in kimberlites. The most distinctive features of the grain boundary zones are (i) the decoupling of Fo and minor elements, as observed in transition zones, (ii) the asymmetric chemical gradients across grain boundaries, with a systematically larger zone in the concave grain and thinner (or absent) zone in the convex grain, and (iii) their association with lobate migrating grain boundaries formed during dynamic recrystallization. Grain boundary zones are often, but not always, lined with margins.

As demonstrated for the transition zones, the gradients observed in the grain boundary zones cannot have resulted from post-crystallization diffusion. The asymmetric distribution of the grain boundary zones across the grain boundaries would require faster diffusion in the concave grains than in the convex grains. Diffusion rates of Fe–Mg and Ni do indeed depend on the crystallographic orientation, but for this to have produced the asymmetry would require a large difference in crystallographic orientation across the grain boundaries. This is inconsistent with the orientations shown in Fig. 2 (e.g. grains 1 and 4), which are not sufficiently different ($\sim$20°) to cause strong differences in diffusion rate (difference of less than a factor of 1·3). Likewise, the width of the grain boundary zone varies within single grains, within which the crystallographic orientation is constant, (misorientation $<$15°, Fig. 2). So, as proposed for transition zones, grain boundary zones do not result from post-crystallization diffusion and thus formed before margin crystallization.

Two observations confirm that grain boundary migration, which is stress-induced, could not have occurred in the kimberlite magma during its ascent to the surface: (1) the tablet-shaped grains, which result from static olivine recrystallization (i.e. annealing) during kimberlite melt ascent (Guéguen, 1979; Nermond, 1994), locally cross-cut the mobile grain boundaries; (2) the margins are free of deformation microstructures; they show only growth dislocation features (Arndt *et al.*, 2010).

We are not aware of previous studies reporting similar asymmetric chemical gradients associated with mobile grain boundaries in natural peridotite xenoliths or in kimberlite nodules. Experimental studies of grain boundary migration in olivine, carbonates and quartz show that asymmetric chemical gradients across mobile grain boundaries develop only when fluid is present (Evans *et al.*, 1986; Nakamura *et al.*, 2005; Ohuchi *et al.*, 2010). The asymmetric grain boundary zones thereby document intergranular percolation of fluid in dynamically deforming lithospheric mantle.

The chemical gradients in the grain boundary zones, which are less than 100 μm in thickness, have been preserved from diffusive equilibration with the host olivine. The sharp Fo gradient between the core and grain boundary zones would not have survived for more than a few days (Figs 7 and 8) at high mantle temperatures (1400°C) and pressures (1 GPa), particularly in the presence of fluids. The high ascent rate of the kimberlite magmas compared with basaltic magmas explains why the chemical gradients are preserved in our kimberlite samples and not in mantle xenoliths. The important conclusion that emerges from this discussion is that fluid or melt percolation in the lithospheric mantle must have occurred shortly before nodule entrainment into the kimberlite magma.

Decoupling of Fo and Ni in kimberlite olivine: a tracer for fluid–peridotite reaction in the lithospheric mantle?

The lithospheric mantle beneath old cratons has a refractory composition dominated by Fo-rich olivine (Boyd, 1989). The mantle beneath the Kaapvaal, Siberia, Slave and Tanzania cratons is unusual in that it contains a relatively high proportion of orthopyroxene, whereas the mantle beneath Greenland is dunitic (Bernstein *et al.*, 2007) and thus resembles the lithology of nodules in kimberlites. However, in marked contrast to the homogeneous composition of olivines in Archean lithospheric peridotites (Fo92–94; Boyd, 1989; Bernstein *et al.*, 2007), the Fo content of olivine in kimberlites varies significantly from nodule to nodule (Fo84–94, this study; Fo85–94, Kamenetsky *et al.*, 2008; Fo84–93, Arndt *et al.*, 2010; Fo88–94, Moore, 2012). This indicates that the nodules in kimberlites cannot simply be equated with the residue left after high-degree melting ($>$40%) as proposed for the shallow cratonic mantle (e.g. Boyd, 1989; Menzies, 1990; Herzberg, 2004; Bernstein *et al.*, 2007). Instead, we propose that the dunitic lithology and the variations in Fo content in the kimberlite nodules were both produced during the elimination of orthopyroxene and other mantle minerals through interaction with silica-undersaturated fluids or melts (Mitchell, 1986, 2008; Kamenetsky *et al.*, 2008; Brett *et al.*, 2009, 2015; Arndt *et al.*, 2010; Russell *et al.*, 2012; Pilbeam *et al.*, 2013; Kamenetsky & Yaxley, 2015).

An important result of our study is the demonstration of the similarity in Fo and minor element contents of olivine in the transition zones, the grain boundary zones, and the core population as a whole (Fig. 4). All three populations show the same chemical range and trends, with large variations in Fo content, whereas Ni, which usually correlates with Fo in olivine, remains relatively constant. The most plausible explanation is that the chemical variability of olivine in these three zones records a similar process.

Experimental and numerical simulations of interaction between silica-undersaturated melt or fluid and lherzolite or harzburgite have demonstrated that the dissolution of pyroxene commonly is coupled with a change in olivine chemistry. The Fo content decreases gradually when approaching the paths of percolating fluids, whereas the mineralogical front that marks the elimination of pyroxene is sharp (Morgan & Liang, 2003; Tursack & Liang, 2012). This interaction leads to the formation of replacive dunite (Kelemen & Dick, 1995) with olivine with variable Fo content (variations of Fo of up to 10 mole units), whereas compatible trace elements, such as Ni, are buffered by the peridotite composition (Tursack & Liang, 2012).

In sample NCR27, we have evidence, at the grain scale, of variations in Fo but near-uniform Ni content in the grain boundary zones adjacent to mobile grain boundaries, which we believe acted as fluid or melt percolation paths. We propose that the unusual decoupling between Fo and Ni within olivine cores, grain boundary zones, and transition zones is a diagnostic feature of interaction between olivine and fluid or melt and, by comparison with chemical gradients in replacive dunites, that this interaction removed the mineral phases other than olivine. The interaction, notably orthopyroxene dissolution, simultaneously modifies the melt composition; in particular, it increases its SiO_2 content (Russell *et al.*, 2012). An important observation is that in high-Fo nodules, the decrease in Fo that we attribute to fluid–rock interaction ends precisely at Fo89, the most magnesian composition observed in olivine margins (Fig. 4). This observation suggests that fluid–rock interaction proceeded until olivine saturation was achieved and thus would pre-date olivine crystallization.

The fluid or melt that interacted with the peridotite was not strictly kimberlitic in composition. The silica-poor carbonatite-like melt previously proposed as 'proto-kimberlite' melt (Kamenetsky *et al.*, 2008; Russell *et al.*, 2012) would be an excellent candidate as it has the low dihedral wetting angle and low viscosity required for efficient percolation along grain boundaries (Minarik & Watson, 1995; Hammouda & Laporte, 2000).

A TEMPORAL FRAMEWORK FOR FLUID–ROCK INTERACTIONS

Mitchell (1986, 2008), Kamenetsky *et al.* (2008), Brett *et al.* (2009, 2015), Russell *et al.* (2012), Pilbeam *et al.* (2013) and Kamenetsky & Yaxley (2015) all proposed that the interaction between peridotite and silica-poor fluid or melt, and the elimination of orthopyroxene, occurred during the transport of the nodules in the kimberlite magma whereas Arndt *et al.* (2010) saw the process happening in the lithospheric mantle prior to xenolith entrainment. Information about the temporal sequence of the processes that occurred in the lithospheric mantle or during the passage of the kimberlite magma from the mantle to the surface comes from textural and chemical features of olivines in sample NCR27, as summarized below.

1. Only a small amount of orthopyroxene assimilation (less than 5 wt %, Table 3) is needed to buffer the Fo content of the margins (Figs 4 and 10). This conclusion removes the requirement that a large amount of orthopyroxene was resorbed during the ascent of the kimberlite magma (15–20%; Le Roex *et al.*, 2003; Mitchell, 2008; Kopylova *et al.*, 2007; Russell *et al.*, 2012; Pilbeam *et al.*, 2013). In our model, the dissolution of orthopyroxene in the mantle gives to the melt and to the crystallized olivine the chemical signature of orthopyroxene, as will dissolution during olivine crystallization.
2. Given that grain boundary zones and transition zones do not result from diffusive equilibration between core and margin but record melt–rock interactions coupled to orthopyroxene dissolution, the position of these zones between cores and margins requires that they formed before crystallization of the margins. This conclusion is supported, first, by the chemical gradients in both zones (together with the cores of the nodules), which indicate that the modification of the olivine composition pre-dated the margin crystallization, and, second, by the fact that grain boundary zones are cross-cut by tablets that developed during magma ascent to the surface.
3. The grain boundary zones document fluid percolation at the grain scale coupled with dynamic recrystallization and grain boundary migration. Dynamic recrystallization cannot have occurred in the low-stress environment of the kimberlite magma during its ascent to the surface (Arndt *et al.*, 2010; Jones *et al.*, 2014) and must have occurred in the solid, deforming lithospheric mantle. The sharp contrasts in composition in the grain boundary zones would have been rapidly degraded by diffusion; the preservation of these zones indicates that fluid percolation occurred shortly (less than a few days) before nodule entrapment into the kimberlite magma.
4. The grain boundary zones are observed in nodules whose compositions range from Fo86 to Fo93, suggesting that they were derived from dunite that was heterogeneous in terms of olivine Fo content. The formation of these zones was contemporaneous with or shortly followed the event that removed any orthopyroxene and other minerals that may have been present and generated the range of olivine compositions in the lithospheric mantle.

In the light of the above observations and interpretations, we believe that peridotite–fluid interaction occurred in the deforming lithospheric mantle, before the dunitic nodules were entrained into the kimberlite melt. At a small scale, the carbonatite-like proto-kimberlite melt percolated along grain boundaries, which migrated simultaneously to accommodate the deformation under high stress. The fluid-assisted

recrystallization led to the development of the grain boundary zones distributed asymmetrically on the two sides of some grain boundaries. Simultaneously, at a scale far greater than the size of the nodules, interactions between peridotite and carbonatite-like protokimberlite melt resulted in the removal of orthopyroxene (and possibly other phases of the peridotites) and the formation of dunite. Within the percolation zones, the olivine composition was uniform at the centimetre scale but variable at a larger scale, depending on the position relative to the percolation zone. The presence of rare low-Fo high-Ni grains could indicate that liquids of different composition—some carbonate-rich, others basaltic—invaded that portion of the lithospheric mantle that was subsequently sampled by the kimberlitic magma. A parallel scenario, implying a kimberlite melt invading the lithosphere, has been invoked to explain the occurrence of megacrysts of garnet, clinopyroxene, orthopyroxene and olivine in the Jericho kimberlite (Kopylova *et al.*, 2009), which resemble our nodules in terms of their polycrystalline nature and textural evidence for recrystallization.

CO_2 exsolution and buoyancy increase resulting from orthopyroxene dissolution (Russell *et al.*, 2012; Kamenetsky & Yaxley, 2015), together with mantle compaction processes (Grégoire *et al.*, 2006), could then have triggered kimberlite melt segregation and ascent. The kimberlite magma entrained dunite xenoliths whose composition records their position in the sheaths of replacive dunite lining the fluid percolation channels in the lithosphere. Disaggregation of xenoliths during their incorporation into the kimberlite melt or during its ascent may be enhanced by fractures or grain boundaries along which the melt previously percolated. Fluid–nodule interaction probably continued at the nodule edges shortly after their entrapment to form the transition zone. When the saturation of olivine was achieved, the margins crystallized without significant concomitant orthopyroxene assimilation.

OLIVINE NODULES IN OTHER KIMBERLITES

Although this study focuses entirely on the Kangamiut kimberlites, many of the same distinctive features are found in kimberlites worldwide. The interpretations we propose here to explain the chemical variations in olivine apply equally well to the monomineralic, polygranular nodules observed in kimberlites from locations such as Majuagaa (Pilbeam *et al.*, 2013), Diavik (Brett *et al.*, 2009; Russell *et al.*, 2012), Ekati, Snap Lake and Botswana (Arndt *et al.*, 2010), and Sover, Monastery and Letseng-la-terai (Moore, 2012). Olivines in kimberlites from other regions (e.g. Udachnaya, Kamenetsky *et al.*, 2008; Lac de Gras, Fedortchouk & Canil, 2004) occur mainly as rounded, sub- to euhedral isolated grains or broken fragments and lack the more distinctive features of the olivines in the locations cited above. However, the lack of associated orthopyroxene and other mantle silicates, and the wide range of Fo contents in olivine cores, suggests that they could also have formed through fluid reaction in the lithospheric mantle. The 'megacrysts' in the Jericho kimberlite described by Kopylova *et al.* (2009) are polymineralic, but they too are proposed to have formed by metasomatism in the lithosphere shortly before kimberlite emplacement.

CONCLUSIONS

We conducted a detailed study of compositions and deformation microstructures in olivine in kimberlite sample NCR27 from the Kangamiut region, Greenland. Monomineralic dunitic nodules make up more than 50% of this sample. The morphology and composition of olivine in the nodules record a combination of processes that occurred during reactive porous flow and metasomatism in the lithospheric mantle, and subsequent xenolith disaggregation and margin crystallization during the ascent of the kimberlite melt.

The composition of olivine in the nodules covers a wide range from high Fo and high Ni (Fo94, 3000 ppm Ni) to low Fo and low Ni (Fo86, 500 ppm Ni), and includes a third, minor population with low Fo but high Ni (Fo88, 2500 ppm Ni). The dunitic lithology and the wide range of olivine compositions result from transformation of mantle peridotite through the dissolution in carbonate-rich liquids of orthopyroxene and other mantle minerals.

Thin margins surround the nodules and the matrix grains. Their compositions, notably the buffering of the Fo content associated with a sharp decrease in Ni, can be reproduced if a high distribution coefficient between olivine and melt is adopted ($D_{Ni} > 20$); concomitant orthopyroxene digestion during magma ascent is not required.

We report chemical gradients across mobile grain boundaries for the first time in a natural peridotite sample. These gradients were preserved from diffusive equilibration because of the short travel time of the nodules in the kimberlite melt. The grain boundary zones are interpreted to have formed by melt–fluid percolation at the grain scale, coupled with dynamic recrystallization in the deforming lithospheric mantle. Grain boundary zones occur in both high- and low-Fo nodules. These relations require that fluid-assisted recrystallization occurred during reactive porous flow and orthopyroxene dissolution, shortly (a few days) before entrainment of the dunite nodules by the kimberlite melt. Because grain boundary zones and high-Fo cores are distributed along similar trends in chemical variation diagrams, we propose that the zoning associated with grain boundaries mimics, on a small scale, the chemical diversity of the dunite that was the source of most of the olivine in the Greenland kimberlites.

ACKNOWLEDGEMENTS

We would like to thank Llewellyn Pilbeam and James Russell, who read and made comments on a first draft of this paper. We also thank Michel Grégoire, Don

Francis and an anonymous reviewer for their very constructive comments, and Marjorie Wilson for her editorial work.

FUNDING

This work was supported by a grant from Labex OSUG@2020 (Investissements d'avenir—ANR10 LABX56). The EPMA facility was purchased and installed at ISTerre via Chair of Excellence grant ANR-09-CEXC-003-01 from the Agence Nationale de la Recherche, France.

SUPPLEMENTARY DATA

Supplementary data for this paper are available at *Journal of Petrology* online.

REFERENCES

Arndt, N. T., Boullier, A. M., Clement, J. P., Dubois, M. & Schissel, D. (2006). What olivine, the neglected mineral, tells us about kimberlite petrogenesis. *eEarth Discuss* **1**, 15–21.

Arndt, N. T., Guitreau, M., Boullier, A. M., Le Roex, A., Tommasi, A., Cordier, P. & Sobolev, A. (2010). Olivine, and the origin of kimberlite. *Journal of Petrology* **51**, 573–602.

Bernstein, S., Kelemen, P. B. & Hanghøj, K. (2007). Consistent olivine Mg number in cratonic mantle reflects Archean mantle melting to the exhaustion of orthopyroxene. *Geology* **35**, 459–462.

Boullier, A.-M. & Nicolas, A. (1975). Classification of textures and fabrics of peridotite xenoliths from south African kimberlites. *Physics and Chemistry of the Earth* **9**, 467–475.

Boyd, F. R. (1989). Compositional distinction between oceanic and cratonic lithosphere. *Earth and Planetary Science Letters* **96**, 15–26.

Brett, R. C., Russell, J. K. & Moss, S. (2009). Origin of olivine in kimberlite: Phenocryst or impostor? *Lithos* **112**, 201–212.

Brett, R., Russell, J., Andrews, G. & Jones, T. (2015). The ascent of kimberlite: Insights from olivine. *Earth and Planetary Science Letters* **424**, 119–131.

Canil, D., & Fedortchouk, Y. (1999). Garnet dissolution and the emplacement of kimberlites. *Earth and Planetary Science Letters* **167**, 227–237.

Chauvel, C., Bureau, S. & Poggi, C. (2011). Comprehensive chemical and isotopic analyses of basalt and sediment reference materials. *Geostandards and Geoanalytical Research* **35**, 125–143.

Clement, C. R. (1982). A comparative geological study of some major kimberlite pipes in the Northern Cape and Orange Free State. PhD Thesis, University of Cape Town, 407 pp.

Dalton, J. A. & Wood, B. J. (1993). The partitioning of Fe and Mg between olivine and carbonate and the stability of carbonate under mantle conditions. *Contributions to Mineralogy and Petrology* **114**, 501–509.

DePaolo, D. J. (1981). Trace element and isotopic effects of combined wallrock assimilation and fractional crystallization. *Earth and Planetary Science Letters* **53**, 189–202.

Dohmen, R. & Chakraborty, S. (2007). Fe–Mg diffusion in olivine II: point defect chemistry, change of diffusion mechanisms and a model for calculation of diffusion coefficients in natural olivine. *Physics and Chemistry of Minerals* **34**, 409–430.

Drury, M. R. & Urai, J. L. (1990). Deformation-related recrystallization processes. *Tectonophysics* **172**, 235–253.

Drury, M. R. & van Roermund, H. L. M. (1988). Metasomatic origin for Fe–Ti-rich multiphase inclusions in olivine from kimberlite xenoliths. *Geology* **16**, 1035–1038.

Drury, M. R. & van Roermund, H. L. M. (1989). Fluid assisted recrystallization in upper mantle peridotite xenoliths from kimberlites. *Journal of Petrology* **30**, 133–152.

Evans, B., Hay, R. S. & Shimizu, N. (1986). Diffusion-induced grain-boundary migration in calcite. *Geology* **14**, 60–63.

Fedortchouk, Y. & Canil, D. (2004). Intensive variables in kimberlite magmas, Lac de Gras, Canada and implications for diamond survival. *Journal of Petrology* **45**, 1725–1745.

Foley, S. F., Jacob, D. E. & O'Neill, H. S. C. (2011). Trace element variations in olivine phenocrysts from Ugandan potassic rocks as clues to the chemical characteristics of parental magmas. *Contributions to Mineralogy and Petrology* **162**, 1–20.

Girnis, A. V., Bulatov, V. K. & Brey, G. P. (2005). Transition from kimberlite to carbonatite melt under mantle parameters: an experimental study. *Petrology* **13**, 1–15.

Girnis, A. V., Bulatov, V. K., Brey, G. P., Gerdes, A. & Höfer, H. E. (2013). Trace element partitioning between mantle minerals and silico-carbonate melts at 6–12 GPa and applications to mantle metasomatism and kimberlite genesis. *Lithos* **160–161**, 183–200.

Grégoire, M., Rabinowicz, M. & Janse, A. J. A. (2006). Mantle mush compaction; a key to understand the mechanisms of concentration of kimberlite melts and initiation of swarms of kimberlite dykes. *Journal of Petrology* **47**, 631–646.

Guéguen, Y. (1977). Dislocations in mantle peridotite nodules. *Tectonophysics* **39**, 231–254.

Guéguen, Y. (1979). Dislocations in naturally deformed terrestrial olivine: classification, interpretation, applications. *Bulletin de Minéralogie* **102**, 178–183.

Hammouda, T. & Laporte, D. (2000). Ultrafast mantle impregnation by carbonatite melts. *Geology* **28**, 283–285.

Hart, S. R. & Davis, K. E. (1978). Nickel partitioning between olivine and silicate melt. *Earth and Planetary Science Letters* **40**, 203–219.

Herzberg, C. (2004). Geodynamic information in peridotite petrology. *Journal of Petrology* **45**, 2507–2530.

Irving (1984). Trace element abundances in megacrysts and their host basalts: Constraints on partition coefficients and megacryst genesis. *Geochimica et Cosmochimica Acta* **48**, 1201–1221.

Jarosewitch, E. J., Nelen, J. A. & Norberg, J. A. (1980). Reference samples for microprobe analysis. *Geostandards Newsletter* **4**, 43–47.

Jones, T. J., Russell, J. K., Porritt, L. A. & Brown, R. J. (2014). Morphology and surface features of olivine in kimberlite: implications for ascent processes. *Solid Earth* **5**, 313–326.

Kamenetsky, V. S. & Yaxley, G. M. (2015). Carbonate–silicate liquid immiscibility in the mantle propels kimberlite magma ascent. *Geochimica et Cosmochimica Acta* **158**, 48–56.

Kamenetsky, V. S., Kamenetsky, M. B., Sobolev, A. V., Golovin, A. V., Demouchy, S., Faure, K., Sharygin, V. V. & Kuzmin, D. V. (2008). Olivine in the Udachnaya-East kimberlite (Yakutia, Russia): types, compositions and origins. *Journal of Petrology* **49**, 823–839.

Kelemen, P. B. & Dick, H. J. B. (1995). Focused melt flow and localized deformation in the upper mantle: Juxtaposition of replacive dunite and ductile shear zones in the Josephine peridotite, SW Oregon. *Journal of Geophysical Research* **100**, 423–438.

Kopylova, M. G., Matveev, S. & Raudsepp, M. (2007). Searching for parental kimberlite melt. *Geochimica et Cosmochimica Acta* **71**, 3616–3629.

Kopylova, M., Nowell, G., Pearson, D. & Markovic, G. (2009). Crystallization of megacrysts from protokimberlitic fluids: Geochemical evidence from high-Cr megacrysts in the Jericho kimberlite. *Lithos* **112**, 284–295.

Laubier, M., Grove, T. L. & Langmuir, C. H. (2014). Trace element mineral/melt partitioning for basaltic and basaltic andesitic melts: An experimental and laser ICP-MS study with application to the oxidation state of mantle source regions. *Earth and Planetary Science Letters* **392**, 265–278.

Le Roex, A. P., Bell, D. R. & Davis, P. (2003). Petrogenesis of Group I kimberlites from Kimberley, South Africa: Evidence from bulk-rock geochemistry. *Journal of Petrology* **44**, 2261–2286.

Li, C., Maier, W. D. & de Waal, S. A. (2001). Magmatic Ni–Cu versus PGE deposits: Contrasting genetic controls and exploration implications. *South African Journal of Geology* **104**, 309–318.

Luth, R. W. (2009). The activity of silica in kimberlites, revisited. *Contributions to Mineralogy and Petrology* **158**, 283–294.

Matzen, A. K., Baker, M. B., Beckett, J. R. & Stolper, E. M. (2013). The temperature and pressure dependence of nickel partitioning between olivine and silicate melt. *Journal of Petrology* **54**, 2521–2545.

Menzies, M. (1990). Archaean, Proterozoic and Phanerozoic lithosphere. In: Menzies, M. (ed.). *Continental Mantle*. Oxford: Oxford University Press, pp. 67–86.

Mercier, J.-C. C. & Nicolas, A. (1975). Textures and fabrics of upper-mantle peridotites as illustrated by xenoliths from basalts. *Journal of Petrology* **16**, 454–487.

Minarik, W. G. & Watson, E. (1995). Interconnectivity of carbonate melt at low melt fraction. *Earth and Planetary Science Letters* **133**, 423–437.

Mitchell, R. H. (1986). *Kimberlites: Mineralogy, Geochemistry, and Petrology*. New York: Plenum, 442 pp.

Mitchell, R. H. (2008). Petrology of hypabyssal kimberlites: relevance to primary magma compositions. *Journal of Volcanology and Geothermal Research* **174**, 1–8.

Moore, A. E. (1988). Olivine: a monitor of magma evolutionary paths in kimberlites and olivine melilitites. *Contributions to Mineralogy and Petrology* **99**, 238–248.

Moore, A. E. (2012). The case for a cognate, polybaric origin for kimberlitic olivines. *Lithos* **128**, 1–10.

Morgan, Z. & Liang, Y. (2003). An experimental and numerical study of the kinetics of harzburgite reactive dissolution with applications to dunite dike formation. *Earth and Planetary Science Letters* **214**, 59–74.

Nakamura, M., Yurimoto, H. & Watson, E. B. (2005). Grain growth control of isotope exchange between rocks and fluids. *Geology* **33**, 829–832.

Nermond, S. (1994). Etude expérimentale de la recristallisation statique et de la cinétique de croissance de l'olivine. PhD Thesis, Université de Paris 7, 204 pp.

Nielsen, T. F. & Sand, K. K. (2008). The Majuagaa kimberlite dike, Maniitsoq region, West Greenland: Constraints on an Mg-rich silicocarbonatitic melt composition from groundmass mineralogy and bulk compositions. *Canadian Mineralogist* **46**, 1043–1061.

Ohuchi, T., Nakamura, M. & Michibayashi, K. (2010). Effect of grain growth on cation exchange between dunite and fluid: implications for chemical homogenization in the upper mantle. *Contributions to Mineralogy and Petrology* **160**, 339–357.

Petry, C., Chakraborty, S. & Palme, H. (2004). Experimental determination of Ni diffusion coefficients in olivine and their dependence on temperature, composition, oxygen fugacity, and crystallographic orientation. *Geochimica et Cosmochimica Acta* **68**, 4179–4188.

Pilbeam, L. H., Nielsen, T. F. D. & Waight, T. E. (2013). Digestion fractional crystallization (DFC): an important process in the genesis of kimberlites. Evidence from olivine in the Majuagaa Kimberlite, southern West Greenland. *Journal of Petrology* **54**, 1399–1425.

Roeder, P. L. & Emslie, R. F. (1970). Olivine–liquid equilibria. *Contributions to Mineralogy and Petrology* **29**, 275–289.

Russell, J. K., Porritt, L. A., Lavallée, Y. & Dingwell, D. B. (2012). Kimberlite ascent by assimilation-fuelled buoyancy. *Nature* **481**, 352–356.

Skinner, E. M. W. (1989). Contrasting Group I and Group II kimberlite petrology: towards a genetic model. In: Ross, J. (ed.) *Kimberlites and Related Rocks: their Composition, Occurrence, Origin and Emplacement. Proceedings of the 4th International Kimberlite Conference. Geological Society of Australia, Special Publication* **29**, 528–544.

Skinner, E. M. W. & Clement, C. R. (1979). Mineralogical classification of southern African kimberlites. In: Boyd, F. R. & Meyer, H. O. A. (eds) *Kimberlite, Diatrems and Diamonds*. Washington, DC: American Geophysical Union, pp. 129–139.

Sweeney, R. J., Prozesky, V. & Przybylowicz, W. (1995). Selected trace and minor element partitioning between peridotite minerals and carbonatite melts at 18–46 kb pressure. *Geochimica et Cosmochimica Acta* **59**, 3671–3683.

Tommasi, A., Vauchez, A. & Ionov, D. A. (2008). Deformation, static recrystallization, and reactive melt transport in shallow subcontinental mantle xenoliths (Tok Cenozoic volcanic field, SE Siberia). *Earth and Planetary Science Letters* **272**, 65–77.

Tursack, E. & Liang, Y. (2012). A comparative study of melt–rock reactions in the mantle: laboratory dissolution experiments and geological field observations. *Contributions to Mineralogy and Petrology* **163**, 861–876.

Urai, J. L., Means, W. D. & Lister, G. S. (1986). Dynamic recrystallization of minerals. In: Hobbs, B. E. & Heard, H. C. (eds) *Mineral and Rock Deformation: Laboratory Studies*. Washington, DC: American Geophysical Union, pp. 161–199.

Wilson, L. and Head, J. W., III (2007). An integrated model of kimberlite ascent and eruption. *Nature* **447**, 53–57.